Three Dimensional Mapping of Lingual Myoarchitecture
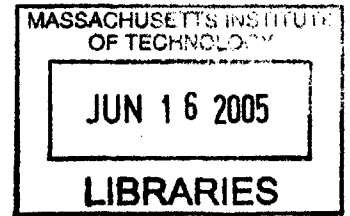
by

Lee Magnusson

Submitted to the Department of Mechanical Engineering
in partial fulfillment of the requirements for the degree of

Master of Science in Mechanical Engineering

at the

MASSACHUSETTS INSTITUTE OF TECHNOLOGY

May 2005

Author ....
Department of Mechanical Engineering
May 5, 2005

Certified by.......
Richard J. Gilbert
Research Scientist, Mechanical Engineering
Thesis Supervisor

Certified by......
Roger D. Kamm
Professor, Mechanical Engineering and Biological Engineering
Thesis Supervisor

Accepted by .....
Lallit Anand
Chairman, Department Committee on Graduate Students
Department of Mechanical Engineering

BARKER

Three Dimensional Mapping of Lingual Myoarchitecture

by

Lee Magnusson

Abstract

The tongue is a structurally complex muscular organ, composed of a continuum of variably aligned intrinsic and extrinsic fibers. An understanding tongue structure and function, both under normal and pathological conditions, requires a complete three dimensional representation of fiber orientations present in the whole tissue. In order to investigate lingual myoarchitecture in the mammalian tongue, we employed several magnetic resonance imaging techniques generally based on direction specific differences in water diffusion. Muscle tissue in particular exhibits significant diffusion anisotropy in the direction of fibers, from which diffusion imaging is able to infer fiber direction. In this thesis research, several diffusion weighted MRI signal acquisition and post processing methods were tested, namely diffusion spectrum imaging (DSI), DSI with tractography, q-ball imaging, diffusion tensor imaging (DTI), and ADC and FA mapping. Each imaging method was evaluated in three ways: 1) finite element simulation using 2D structures to model the diffusion environment in an idealized situation, 2) MRI of microfluidic phantoms to quantify the effects of experimental conditions with a known diffusion environment, and 3) MRI of biological tissue, namely ex vivo cow and in vivo human tongues. The results demonstrated the capacity of DSI alone and in association with tractography to depict complex intravoxel and intervoxel fiber populations, in which a voxel is a 1-5 mm cubic imaged volume. In particular, our findings have identified and characterized on a structural basis a novel set of interwoven fiber populations. Future work will be directed to defining the mechanical significance of these interwoven fiber populations in carrying physiological tissue deformations.

Thesis Supervisor: Richard J. Gilbert
Title: Research Scientist, Mechanical Engineering

Thesis Supervisor: Roger D. Kamm
Title: Professor, Mechanical Engineering and Biological Engineering

Acknowledgments

I would like to acknowledge the following entities for their assistance in helping me get me where I am today and assistance with research. In no particular order, Alex de Crespigny for helping with small-bore scanner and providing assistance with data processing; Ruopeng Wang for his excellent DSI processing and visualization programs; Van J. Wedeen for his willingness to teach me the fine details of DSI and diffusion imaging as well as making beautiful presentations; my advisor Richard J. Gilbert for all the stuff that advisors do including providing direction, helping with writing this thesis, sending me to conferences, providing lunch, and teaching in the form of basic knowledge, writing, presenting, and teaching others; Kristopher Ryan Beevers for his help with writing and LaTeX; Mike Venzke for writing computer programs; [friends] for its informative and amusing messages; Prof. Roger Kamm for being the department thesis reader and providing helpful comments; Gene Ray for understanding the time cube; Thomas Benner for his help on the clinical scanner and his willingness to dispose of old tissues; Lisa Liu for working on her thesis at the same time I am; Doug, Jeff, Ben, Andy, Sonia, Mike, Mike, Peter, Austin, Dave, Alan, Nic, Conor, Rory, and probably some others for being friends; Mother and Father for not hassling me too much, and standard parent arguments; Matt and Jess for their contributions; MIT for providing helpful and informative classes; Prof. Sanford S. Sternstein for taking me on for an undergraduate research project and encouraging further academic endeavors; and Athinoula A. Martions Center for Biomedical Imaging for providing scanning facilites. I hope I didn't forget too many others.

Contents

List of Figures

List of Tables

Chapter 1

Introduction

Muscle tissues in general make use of a large variety of fiber arrangements, optimized for a specific application. The tongue in particular exhibits an enormous amount complexity, and as such, is capable of attaining a near limitless number of possible deformations. Due to limited skeletal attachment the musculature of the tongue must, in addition to deformation, provide structural support through stiffening. This muscular function is classified as hydrostatic, since changes in shape occur with little or no change in volume. The tongue has thus has been likened with other organs in nature called muscular hydrostats.

The understanding of tongue structure and function requires a complete three-dimensional representation of fiber orientations present in the whole tissue. Traditional multi-slice histological methods for determining fiber orientations are lacking due both in difficulty in extrapolating to three dimensions and the invasiveness of the procedure. Magnetic resonance imaging (MRI) is an inherently safe and noninvasive procedure and hence is considered for application in determining tongue myoarchitecture.

1.1 Mammalian lingual myoarchitecture

The tongue body is composed of many different types of tissue, including epithelial, glandular, connective, and muscular. However, it is the muscular tissue that affords

the tongue its impetus for deformation, and hence will be described more rigorously. The mammalian tongue is traditionally characterized as several muscles divided into two groups, intrinsic and extrinsic [2, 3, 37]. *Intrinsic* muscles are myofiber populations wholly contained within the body of the tongue, unconnected to any external bony attachments. In contrast, *extrinsic* muscles have one bony attachment outside the tongue proper. The intrinsic muscles include the superior and inferior longitudinalis, the transversus, and the verticalis muscles. The extrinsic muscles include the genioglossus, the hyoglossus, the styloglossus, and the palatoglossus muscles. The tongue rests on a muscular floor composed of the geniohyoid muscle, which runs in the mid-sagittal plane from the mental spine of the mandible to the body of the hyoid bone; and the mylohyoid, which runs from the mylohyoid line of the mandible to the raphe and body of the hyoid bone. This precise locations of these muscles in this traditional characterization of myoarchitecture are shown Figure 1-1(a) and described in more detail below.

The intrinsic muscles of the anterior tongue include the superior longitudinalis muscle, which runs parallel to the dorsal surface of the tongue below the thick epithelium. Below this myofiber population lies the intrinsic core of the tongue. This region contains sequential sheets (in the coronal plane) of superior-inferiorly and medial-laterally directed fibers - the verticalis and transversus muscles, respectively. Below this core layer is the inferior longitudinalis muscle. The transversus, verticalis, and longitudinalis muscles also extend to the posterior tongue, where they are merged with the extrinsic muscles.

The extrinsic muscles enter the tongue proper from a superior direction (palatoglossus), postero-superior direction (styloglossus), postero-inferior direction (hyoglossus) and antero-inferior direction (genioglossus). The genioglossus is a notably large muscle that originates at the mental spine of the mandible and enters the tongue from below, in a fan-like projection. This muscle comprises the bulk of the posterior tongue. We emphasize the importance of the idea that the extrinsic muscles merge seamlessly with the intrinsic musculature, confounding the simplified characterization of distinct muscular populations within the tongue. For example, as the genioglossus muscle

fans superiorly into the tongue's intrinsic core, its fibers merge with verticalis muscle fibers, sometimes extending all the way to the superior longitudinalis [40]. Thus, more recent conceptualizations of lingual myoarchitecture, suggest that partitioning of the tongue into nominally discrete muscles may be inaccurate, since lingual fibers overlap and merge so extensively. Figure 1-1(b) shows a more recent reconstruction of the tongue when considering the structure as a continuum.

Reflecting the diversity of fiber organization and mechanics of the tongue, there is also great importance in understanding the structure of the relevant motor units. Since the distribution of muscle fibers within such motor units impact upon the patterns of local contraction, motor unit architecture should be considered a central attribute of hydrostatic function. The longitudinalis fibers of the tongue appear to be comprised mostly of in-series muscle fibers [29]. This finding has been confirmed by single motor unit EMG showing motor unit function localized to a fraction of the muscle's length in situ [36]. As such, the transmission of force along a single such motor unit is highly dependent upon the contractile state of other in-series motor units [13,14]. The structure of motor units within the intrinsic core, or at the interface between extrinsic and intrinsic core fibers, is less clear. The core muscles are composed of alternating sheets of vertical and transverse fibers, yet is appears unlikely that single sheets are consistent with single motor units. These regions manifest terminal nerve branches, but these branches appear to distribute to both the vertical and transverse muscle fibers in adjacent sheets, suggesting the possibility that motor unit territory may in fact overlap between vertical and transverse muscle fibers. Moreover the terminal branches have small anastomotic connections suggesting that axons extend longitudinally to encompass more than a single transverse/vertical sheet. Thus, the exact structure of the motor units within the core region is unclear, and may be unique to their function within a muscular hydrostat.

Both intrinsic and extrinsic lingual fibers may be arrayed within the tissue to generate a large variety of shapes by virtue of the tissue's hydrostatic properties. The structural components of each element may further be considered as a hierarchical organization of individual myofibers, collagen-delimited fiber bundles, allowing
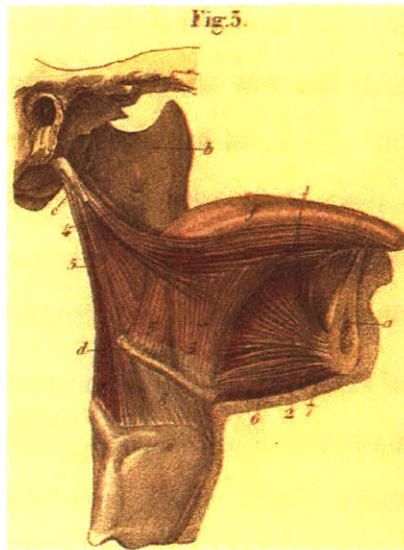
(a)
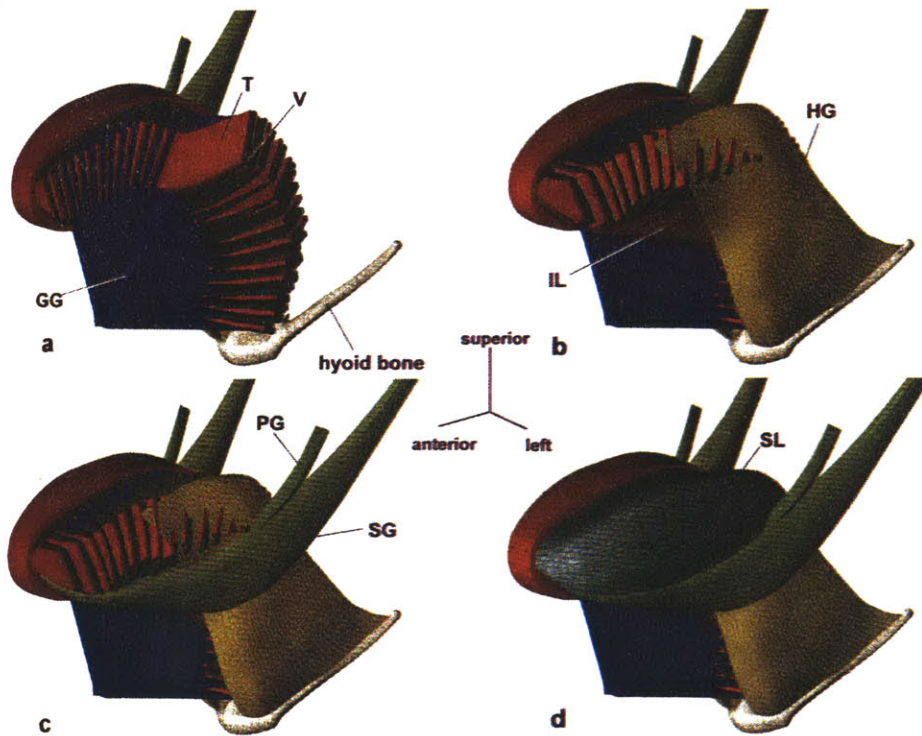
(b)

Figure 1-1: a) Classical depiction of human tongue myoarchitecture [7]. Bones: a - mandible, body, b - mandible, ramus, c - styloid process, d - hyoid bone, e - larynx, f - lingula. Muscles: 1 - m. lingualis, 2 - m. genioglossus, 3 - m. hyoglossus, 4 - m. styloglossus 5 - m. stylopharyngeus, 6 - m. geniohyoideus, 7 - m. mylohyoideus (s. digastricus), 8 - thyrohyoid membrane. b) Reconstruction of human tongue myoarchitecture when viewed as a continuum of fibers [40]. IL - inferior longitudinal muscle, SL - superior longitudinal muscle, HG - hyoglossus, SG - styloglossus, PG - palatoglossus

the tissue to be defined simultaneously at macroscopic (discrete regions within a tissue) and microscopic (individual myofibers and fiber bundles) levels of resolution. Diversity of physiological function may then be derived from the anatomical relationships between fibers and fiber bundles, as well as regional differences of innervation, excitation-contraction coupling, and muscle fiber type [12].

1.2 Movements of the mammalian tongue

The tongue plays a major role in voluntary movements of vocalization, mastication, swallowing, and in humans, complex speech patterns. The exact means that it is able to create these motions is due to its unique muscular composition with limited bony attachment. Our core hypothesis is that the human tongue functions as a variant of a muscular hydrostat [19,33,35]. Muscular hydrostats are characterized by myofibers both providing the structural support and the motion itself, thus eliminating the need for bony support in the form of either an endoskeleton or exoskeleton. By definition, a hydrostat has a isochoric, or constant volume, requirement. Thus, contraction in one or two directions will provide a commensurate opposite length change in a third orthogonal direction.

The term hydrostat was first used to characterize the ability of animals (vermiform and polyps) which lack any skeleton, to create motion. It was later discovered that various properties which explained the movement of these completely hydrostatic animals could be used to explain the motions of organs in more complex species. Examples of hydrostatic organs are the tongue, the trunk, and tentacles. Each of these organs has its own unique set of fiber orientations. In order to categorize orientation, Kier defined three general orientations for fibers, 1) perpendicular to the long axis, 2) parallel to the long axis, and 3) helical or oblique to the long axis of the organ [19]. Muscular hydrostats have been described which exhibit either one, two or all three of these orientations within a single organ.

The chambered nautilus was shown to exhibit an inner core of radially aligned muscle fibers, surrounded by and interdigitating with a thick layer of longitudinal
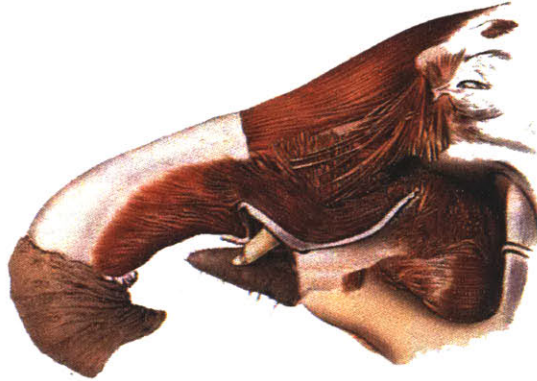
Figure 1-2: The surface muscle structure of the elephant trunk. The limited bony attachment of the trunk enables the characterization of its movements as hydrostatic. The surface helical muscle alignment is visible on the trunk.

muscle, and finally enclosed in a thin obliquely oriented sheath [19]. The elephant trunk is composed of a similar arrangement to the chambered nautilus, but with different proportions and a hollow inner nasal cavity [1]. The elephant trunk muscle structure is illustrated in Figure 1-2. The octopus is comprised of inner transverse muscle surrounded by longitudinal muscle and finally by by two layers of oblique muscles of opposite handedness. The tentacles of the squid contain a transverse core surrounded by longitudinal muscle and then a thin layer layer of circumferential muscle and finally another thin layer of helical muscle. The anterior tongue of the monitor lizard has a large longitudinal muscle core surrounded by circumferential muscle layers [19]. Last, for the case of the anterior mammalian tongue, the are core longitudinal/vertical muscle layers, surrounded by longitudinal muscle [2,3,19,32,37]. The core tongue musculature is shown schematically in Figure 1-3. There are a large number of different orientational arrangements possible in muscular hydrostats; these gross changes in structure relate to different properties and motions.

The entire set of motions of the tongue are a hybrid combination of hydrostatic deformations and externally supported ones. Movements of the anterior tongue (including protusion, bending, and stiffening) are hypothesized to be completely hydrostatic. Protrusion occurs through combined contraction of transversus and verticallis fibers [31]. Through the hydrostatic hypothesis, this co-contraction must produce a
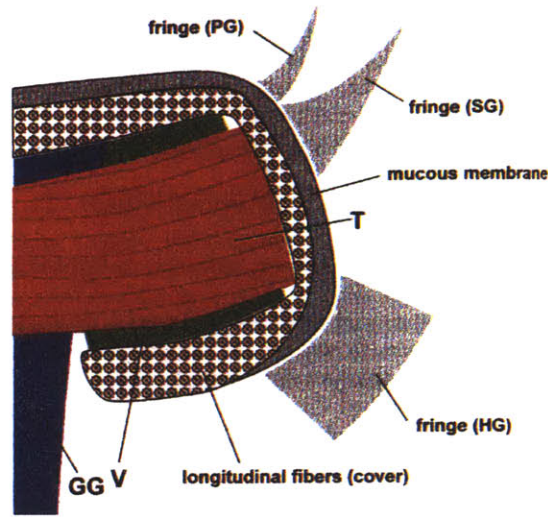
Figure 1-3: Schematic representation of anterior core tongue musculature in an axial view. Crossing transversus (T) and verticalis (V) muscles oppose the motion of the surrounding longitudinal (L) sheath [40].

longitudinal expansion to maintain the constant volume condition. Bending however, fundamentally only requires contraction of a single longitudinal population. Single population contractions that create bending would be either superior or inferior longitudinal fibers for sagittal bending, or latterly situated longitudinal fibers for horizontal bending. However, strain imaging measurements of the tongue in-vivo have shown contraction of transverse populations in addition to longitudinal contraction during sagittal tongue bending. This co-contraction is explained by the increased curvature possible [32], and potentially due to transverse fibers creating a stiffened structural support for deformation. More complicated intrinsic deformations necessary in speech and swallowing are not well understood.

Externally supported movements modify the shape and position of the tongue from external attachment points. For example, the genioglossus is involved with respiration and it contracts with each inspiration, opening the airway. Similarly, the genioglossus plays an important role in swallowing in which shape is modified to accommodate a bolus and sequential contractions produce retrograde propulsion. The hyoglossus and styloglossus also contribute in swallowing and other deformations, but the precise roles are not clear, as these two muscles merge extensively with intrinsic musculature.

19

1.3 Characterization methods

Deriving accurate information regarding lingual muscle fiber orientation has classically relied on meticulous dissection and multi-slice H&E stains, an approach, which is both laborious and ill-posed in the case of the tongue. The difficulty stems from the inability of histology, an inherently two-dimensional technique, to resolve through plane fiber angle deviation. Moreover, accurately assembling these planar local data into a coherent and complete three-dimensional atlas poses further problems [24]. Histology is also invasive, requiring the sacrifice of the sample. This particular characteristic is rather prohibitive to studying human subjects. With these caveats in mind, past in vitro investigations have been very helpful in outlining the gross configuration of lingual musculature. Miyawaki performed a detailed observational study in which the tongue was pretreated in xyrol, thereby elucidating fiber directionality [26]. Other investigations have utilized conventional histologic and histochemical techniques to derive geometrical fiber interrelationships, musculature population percentage, fiber type, and innervation [12, 29, 40].

MRI is an excellent method for investigating the properties of biological tissue including the tongue as shown in Figure 1-4. MRI is extremely flexible and there are many different techniques to obtain contrast or quantitative data overlaid on tomographic images, such as temperature, velocity fields, strain fields, brain activation, and diffusion. The two main MRI techniques used in the tongue have involved either strain or diffusion imaging. Strain imaging is typically associated with functional imaging of muscle tissue during different deformations. Diffusion imaging acquires images only in the relaxed configuration and provides muscle fiber orientations and structure. The relationship between the two techniques is generally that strain acts along the lines of muscle orientation, but thorough understanding would require constructing a model of the tongue.

Strain imaging is possible with two different MRI techniques. The first technique, tagged imaging, uses an orthogonal grid of saturated magnetization planes normal to the imaging plane. This results in an MRI image with a darkened grid of lines,

Figure 1-4: An MRI of the human tongue. This is a mid-sagittal plane through the head.

typically spaced 2.5-5 voxels apart, where a voxel is a three dimensional imaging volume. After the grid is applied to the tissue, two images are taken, first in the undeformed structure, and then after subsequent deformation. A tagged grid in the deformed configuration of a tongue is shown in Figure 1-5(A). Points are marked at the intersection of grid lines in both images and from the change in shape of the points a 2D strain tensor is calculated. 3D strain analysis is possible with assumptions about the tissue properties (such as incompressibility), and with simultaneously imaging of adjacent slices. The results of such a calculation are shown in the case of sagittal tongue bending in Figure 1-5(C-F) [31]. The second strain imaging technique, phase contrast imaging, works by applying velocity encoding gradients. From the phase data of images it is possible to obtain a velocity tensor and a strain tensor by integrating over time. Phase contrast imaging may provide a better method for fundamentally understanding muscle activation, but has not be applied to date in the tongue. The scope of this thesis is however, limited only to structural imaging possible with diffusion and will not further consider strain imaging.

Structural imaging of myofiber architecture has been mainly performed with diffusion weighted MRI techniques. This thesis is formed on the basis of previous diffusion
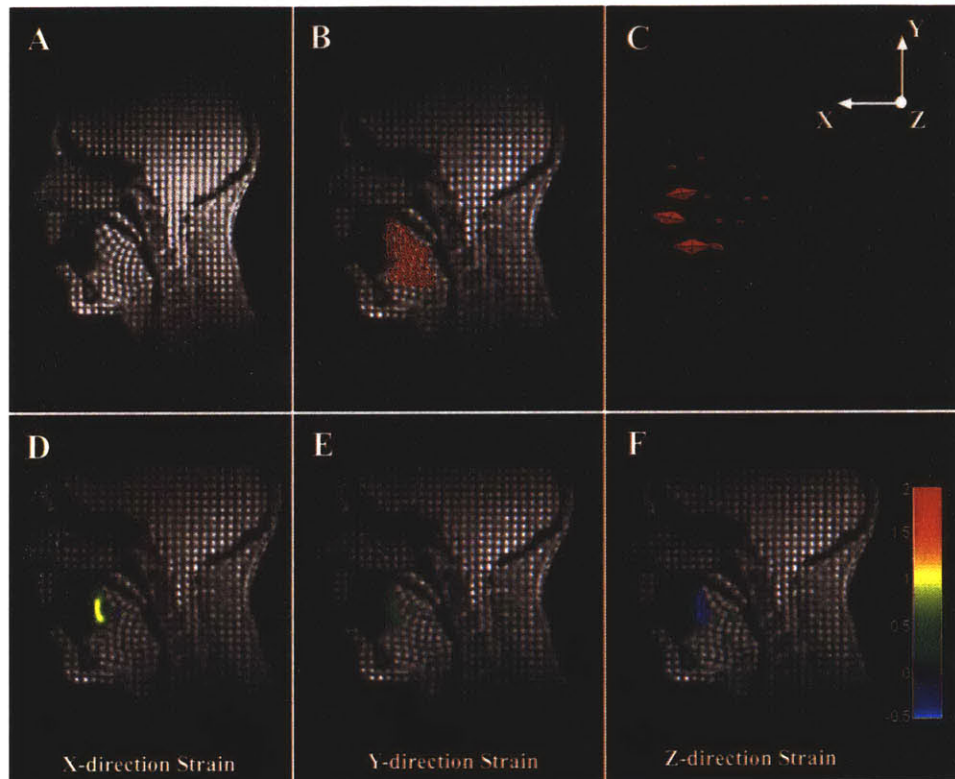
Figure 1-5: A mid-sagittal analysis of the human tongue in sagittal bending to the hard palate using MRI tagged imaging strain data. (A) Deformed grid imaged after tongue bending. (B) Triangular finite element mesh associated with this motion. Each element's entire 3D strain tensor was represented in (C) and exhibited the posterior and inferior regions of the tongue to be strain free. (D), (E), and (F) relate the x, y, and z normal strain components of the strain tensor respectively. x-direction and z-direction strain increased and decreased radially from the center of curvature, respectively [31].

imaging techniques used in the tongue, as well as new more accurate techniques in the presence of complex myoarchitecture. Diffusion imaging techniques use the ability of MRI to obtain diffusion weighted images. Diffusion weighted images are typical MRI images in that they capture the tomographic images overall structure of the tissue with typical resolutions of 1-5 *mm*. However, unlike typical MRI images, they have voxel intensities that are attenuated by the magnitude of diffusion in the direction of an applied diffusion weighting gradient. The diffusion weighting gradients can be applied in any 3D vector direction and magnitude; this diffusion gradient vector space is termed q-space. Owing to the fact that maximal diffusion occurs orthogonal to the short axis of most fiber-type cells, diffusion measurements can be used to derive information regarding three-dimensional fiber orientation in situ [6, 12, 16, 18, 28, 47]. Previous MRI investigations of tongue myoarchitecture have relied on a method for extracting a three dimensional, second order tensor for diffusion in each imaging voxel, called diffusion tensor imaging (DTI). These tensor fields produce a virtual anatomical display of the tongue [15, 44], which is in close agreement with the detailed dissection study of Miyawaki [26]. Diffusion tensor imaging successfully parceled the tongue into its principal muscular components, as identified by principal fiber direction and diffusion anisotropy. Figure 1-6 shows a diffusion tensor field obtained from DTI on a cow tongue.

There is however, a core problem with DTI in that it assumes that biological diffusion in the voxel conforms to an anisotropic Gaussian diffusion model, which is representable as a diffusion tensor with six independent parameters. Using this model assumes that there is only one primary myofiber population in the voxel and thus is unable to provide precise angular relationships for crossing or diverging fiber populations [15, 30, 44]. High angular resolution (HARD) diffusion imaging techniques were designed to overcome this shortcoming. In this research, several diffusion weighted MRI signal acquisition and post processing methods were tested, namely diffusion spectrum imaging (DSI), DSI with tractography, q-ball imaging, diffusion tensor imaging (DTI), apparent diffusion coefficient (ADC), and fractional anisotropy (FA) mapping. The most fundamental of these imaging techniques is DSI in which it

23
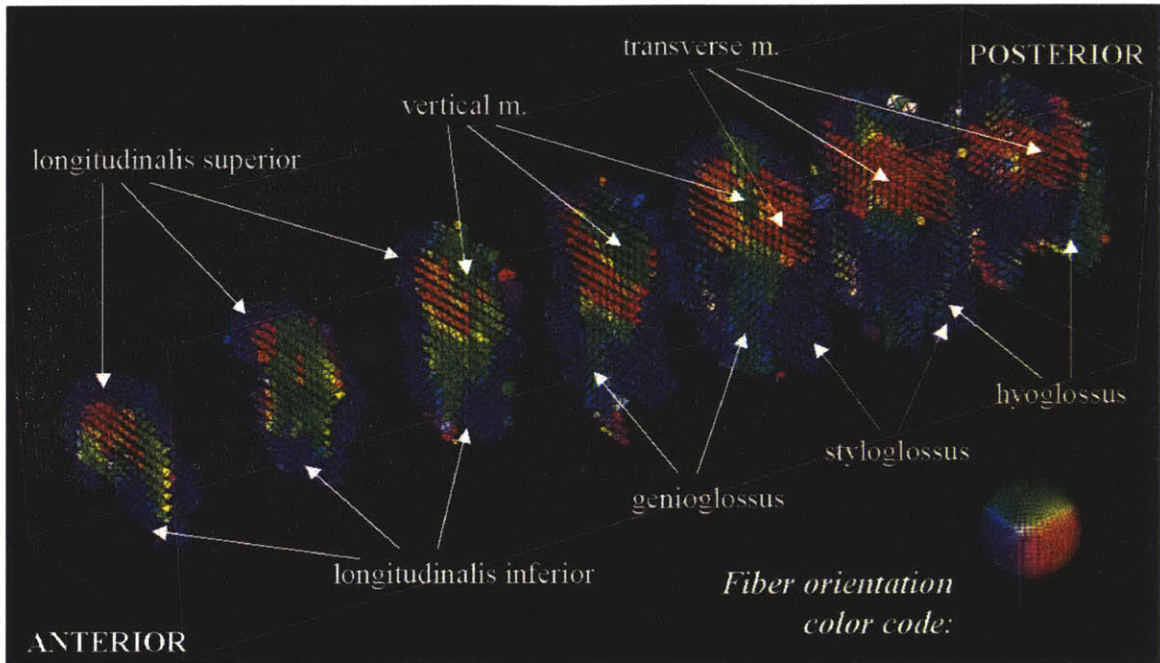
Figure 1-6: 3D multislice diffusion tensor MRI of the bovine tongue. Coronal slices comprising the bovine tongue obtained by diffusion tensor imaging, with muscle components identified. At each voxel is placed an octahedron whose shape approximates the local diffusion tensor. The fiber orientation corresponds to the octahedron's long axis and its color the 3D orientation. The color-code is shown in the color sphere (inset lower right). The sheath consisting of superior and inferior longitudinal muscles is blue, corresponding to its longitudinal fiber orientation, and the tongue core is red and green, corresponding respectively to horizontal and vertical fiber orientations, whereas the extrinsic genioglossus and hyoglossus muscles are oblique, and thus coded blue-green [31].

24

samples all of q-space. In DSI, the gradients are applied in directions corresponding to a filled sphere of points on a Cartesian grid in q-space. Data obtained in q-space has a Fourier transform relationship to diffusion space, where diffusion space is a 3D probability function of random water displacement. This displacement function (PDF) represents the average *microstructure* within each voxel, because typical diffusion distances are 10-20 μm, which are two orders of magnitude higher in resolution than the MRI image voxels. Peaks in the PDF represent directions of less restricted water diffusion, which to correlates with the directions of one or more myofiber populations in the voxel. DSI and as well as the more limited q-space acquisitions are considered in detail in this thesis.

1.4   Thesis organization

The remainder of this thesis is organized as follows: Chapter 2 provides an introduction to magnetic resonance imaging (MRI) and describes the theoretical basis for diffusion imaging. Chapter 3 then presents the several acquisition and post-processing methods used in diffusion imaging that enable imaging and reconstruction of complex three dimensional structures. Chapter 4 presents simulated and experimental validation for the ability diffusion imaging to resolve complex myoarchitecture. Chapter 5 presents the results of several diffusion imaging experiments on ex-vivo cow tongues and esophagi. The thesis ends with Chapter 6, which concludes and provides future directions.

Chapter 2

Magnetic Resonance Imaging of Diffusion

Magnetic Resonance Imaging (MRI) is a non-invasive imaging technique which utilizes the nuclear magnetic resonance phenomenon to produce an image [20, 23]. By applying a strong homogeneous magnetic field in addition to pulsed magnetic field gradients, nuclear spins acquire a spatially dependent frequency and phase. The time domain signal acquired thus has a Fourier transform relationship to spatial dimensions. This Fourier transformed data is an image of (typically) water in the scanned sample. Additionally MRI has the ability to obtain contrast, which is its fundamental strength in discriminating different biological conditions. One such mechanism for contrast is diffusion weighting, in which the signal intensity is attenuated quantitatively by diffusion in a specific diffusion weighting direction. The quantitative understanding of diffusion is further used to interrogate microstructural features, such as average fiber orientation in an imaging voxel. This chapter presents an overview of the fundamentals of MRI, presents some of the physics of diffusion, and then explains how the MRI signal is affected in the presence of diffusion.

2.1 Nuclear magnetic resonance

Subatomic particles have have an intrinsic property called spin angular momentum (or simply referred to as spin). This concept tries to draw from well understood dynamics of angular momentum on a macro scale in a continuum, but also has unique properties. Unlike macro scale angular momentum which is able to change in magnitude and direction by interaction with the environment, spin always has a constant magnitude but can still change in direction. The constant magnitude is a function only of the structure. For a proton atom alone, as is the case of hydrogen (or water) imaging that comprises most of MRI, the spin is 1/2, and is much better at producing signal than heavier elements because the lower amount of electron shielding. The magnetic moment of a proton ($\vec{\mu}$) is proportional to the spin ($\vec{J}$).

$$\vec{\mu} = \gamma \vec{J}$$
$$\gamma = 2.675 \times 10^8 \frac{\text{rad}}{\text{T} \cdot \text{s}}, \tag{2.1}$$

where γ is the gyromagnetic ratio for a proton. The gyromagnetic ratio for protons is relevant because it is the same constant for single proton hydrogen atoms and water (H_2O, again, what is typically what is imaged in MRI). Biological tissue is composed mainly of water and thus MRI imaging in biology is sometimes referred to as imaging hydrogen, imaging protons, or imaging spins.

The nuclear magnetic resonance phenomenon was discovered independently by Bloch and Purcell in 1946 [8, 34]. They observed the precession of spins around a magnetic field. The apparatus they constructed was designed to apply a strong homogeneous magnetic field in the $\hat{z}$ direction and an oscillating magnetic field in the xy plane. It was observed that when the spin, which is proportional to the magnetic moment, direction was rotated down into the xy plane, the magnetic moment rotated in the xy plane at the Larmor frequency. This produced an oscillating response from the protons called precession as is given by equation (2.2).

$$\nu = \gamma |\vec{B}| \tag{2.2}$$

ν is the Larmor precession frequency in the xy plane, and $|\vec{B}|$ is the magnitude of the magnetic field. This rotating magnetic moment produces an associated rf signal which is picked up by a receiving coil.

Differentiating equation (2.1) with respect to time and substituting in that the time derivative of angular momentum is torque (from Newton's second law of motion), and torque is given by $\vec{\mu} \times \vec{B}$,

$$\frac{d\vec{\mu}}{dt} = \gamma \vec{\mu} \times \vec{B}. \tag{2.3}$$

In MRI, the magnetic moment is put in a uniform strong magnetic field in the $\hat{z}$ direction. With this constraint on $\vec{B}$, the magnetic moment equation of motion (2.3) is very similar to mechanical precession of a gyroscope about a point in a gravitational field. Thus the magnetic moment precesses in the xy plane about the z direction, and would do so indefinitely in the absence of externally applied forces.

The rf signal that is readily acquired externally with a receiving coil is the sum of all of the magnetic moments $\vec{\mu}$ at their respective frequencies, producing the overall magnetization vector $\vec{M}$ per unit volume.

$$\vec{M} = \frac{1}{V} \sum_{\substack{\text{protons} \\ \text{in } V}} \vec{\mu} \tag{2.4}$$

Then equation (2.3) is summed over a volume, thus writing the equation of motion in terms of $\vec{M}$.

$$\frac{d\vec{M}}{dt} = \gamma \vec{M} \times \vec{B}_{ext} \tag{2.5}$$

This equation represents non-interacting protons, and thus the absence of external forces, in which $\vec{B}_{ext}$ is a externally applied magnetic field and $\vec{M}$ precesses in the xy plane indefinitely. However, this is not the the case in real conditions, due to protons interacting with their surroundings in which magnetization will attempt to return exponentially to its stable equilibrium aligned with the z axis. This phenomenon is called relaxation for which there are two important time constants; T_1 is the time constant for relaxation in the z direction and T_2 is the time constant for relaxation in the xy plane. Bloch further modified the equation of motion (2.5) to account for

these two phenomenological time constants.

$$\frac{d\vec{M}}{dt} = \gamma \vec{M} \times \vec{B}_{ext} + \frac{1}{T_1}(M_0 - M_z)\hat{z} - \frac{1}{T_2}\vec{M}_\perp \qquad (2.6)$$

where we have assumed that there is a large static magnetic field applied in the z direction. M_z is the component of magnetization in the z direction, M_0 is z direction component of the low energy state in which $\vec{M}$ is aligned with the z axis, and $\vec{M}_\perp$ are the components of $\vec{M}$ in the xy plane. This modified equation of motion correlates with the concept of a mechanical gyroscope precessing to a lower energy state, i.e. aligning with gravity in the negative direction. In practice, T_2 is always shorter than T_1 and typical physiological values for muscle are $T_2 = 50 \ ms$ and $T_1 = 900 \ ms$. This vector equation of motion is separable in to two uncoupled ordinary differential equations, using a complex number representation in the xy plane.

$$\frac{dM_+}{dt} = -i\omega_0 M_+ - \frac{M_+}{T_2}$$
$$\frac{dM_z}{dt} = \frac{M_0 - M_z}{T_1} \qquad (2.7)$$
$$M_+ \equiv M_x + iM_y \qquad \omega_0 \equiv \gamma \vec{B}_0$$

These equations are readily solved for this static z direction magnetic field case.

$$M'_+(t) = e^{i\omega_0 t - t/T_2} M_+(0)$$
$$M'_z(t) = M_z(o)e^{-t/T_1} + M_0 \left(1 - e^{-t/T_1}\right) \qquad (2.8)$$

A sample trajectory of the magnetization vector from an initial condition in the xy plane and evolution of state given by equation (2.8), is shown in Figure 2-1.

Written in terms of a rotating reference frame in the xy plane at the Larmor frequency, $x'y'$, Bloch derived the following equations to simplify understanding and presentation of the data. Assuming that $\vec{B}_{ext}$ now takes on a form $\vec{B}_{ext} = B_0\hat{z} + B_1\hat{a}'$, where $\hat{a}$ is unit vector in the $x'y'$ plane that represents the direction of the applied
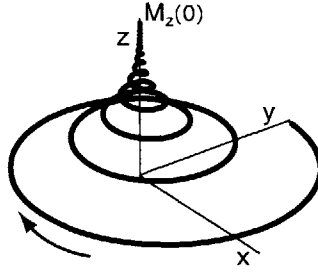
30

Figure 2-1: Trajectory of the magnetization vector. Inward spiral is due to T_2 relaxation and return to $M_z(0)$ on the z axis is due to T_1 relaxation. The actual frequency of oscillation in the xy plane with respect to relaxation times is much higher then depicted here.

$\vec{B}_1$ field.

$$\frac{M_{+'}}{dt} = (\vec{\omega}_{1_{x'}} + i\vec{\omega}_{1_{y'}})M_z - i\Delta\omega M_{+'} - \frac{M_{+'}}{T_2}$$

$$\frac{M_z}{dt} = -|\vec{\omega}_1||M_{+'}| + \frac{M_0 - M_z}{T_1}$$

$$\omega_0 = \gamma|\vec{B}_0| \qquad \vec{\omega}_1 = \gamma\vec{B}_1$$

$$\Delta\omega \equiv \omega_0 - \omega$$

(2.9)

Through the manipulation of the $\vec{B}_1$ field and application gradients of z direction magnetization to manipulate $\vec{B}_0$, these equations form the basis for all of MRI.

2.2 Diffusion theory

To discuss how the NMR signal is affected by diffusion, we first describe the theory of diffusion. Diffusion, as was first noted by Brown, describes the random motion of molecules [9]. Diffusion occurs in solids, liquids, and gases in single or multi-phase mixtures. In single phase diffusion, molecules move about within the same phase, and is called homogeneous or self-diffusion. The form of MRI diffusion imaging used images only water molecules, so it is considered self-diffusion in a medium with boundary conditions specific to the structure. Since water molecules move about randomly throughout their structure of boundary conditions, it is possible to acquire information about their structure based on knowledge of the water diffusion in that

31

area.

The partial differential equation for diffusion is:

$$\frac{\partial P(\vec{r}, t)}{\partial t} = -\nabla \cdot \vec{v} P(\vec{r}, t) + \mathbf{D}\nabla^2 P(\vec{r}, t), \tag{2.10}$$

where $P(\vec{r}, t)$ is the concentration at $\vec{r}$ at time t, $\vec{v}$ is the time derivative of $\vec{r}$ is a coherent velocity term, $\mathbf{D}$ is a second order tensor of diffusion coefficients, and ∇^2 is the divergence of the gradient operator. To understand how knowledge of the diffusion concentration relates to structure, a number of example solutions of equation (2.10) are considered.

2.2.1   Infinite boundary conditions

The diffusion kernel is the solution of the diffusion equation 2.10 to a delta function initial condition with infinite medium boundary conditions, where a delta function $(\delta(\vec{r}))$ is defined by:

$$\int \delta(\vec{r})d\vec{r} = 1 \text{ and } \int f(\vec{r})\delta(\vec{r})d\vec{r} = f(\vec{0}) \tag{2.11}$$

The delta function is thus an impulse of infinite height and unit volume, located at the origin. The concept of the delta function is to have an initial condition with a volume of unity all concentrated at a point. A 2D illustration of the delta function is shown in Figure 2-2(a). The solution of the diffusion equation to this condition in an isotropic medium is given by a Gaussian distribution.

$$P(\vec{r}, t) = \frac{1}{\sqrt{|\mathbf{D}|}(4\pi t)^{3/2}} \exp\left(\frac{\vec{r} \cdot \mathbf{D}^{-1}\vec{r}}{2t}\right). \tag{2.12}$$

Figures 2-2(b-d) show the transient response for this solution. The diffusion tensor used in the solution had a 3:1 ratio of eigenvalues, meaning that diffusion occurred more readily in one maximal direction, and was minimal in the orthogonal direction to the maxima. This solution is a gross simplification of the boundary conditions seen

32
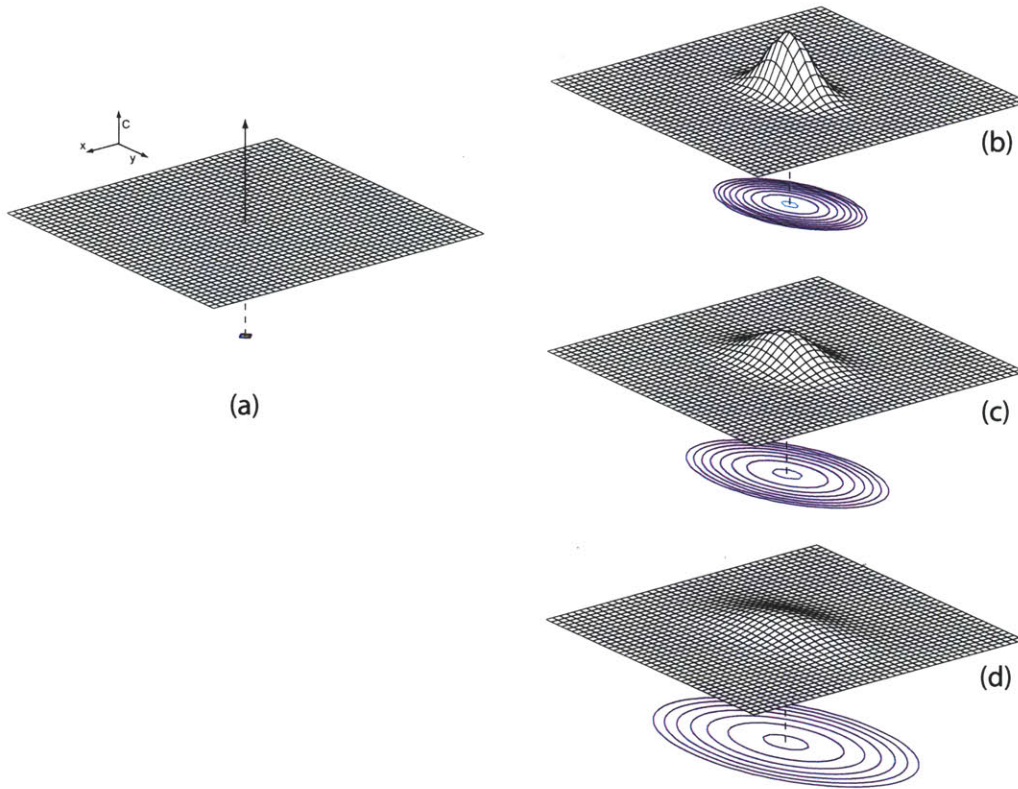
Figure 2-2: Two dimensional anisotropic Gaussian distribution. (a) The initial point delta function in concentration. (b-d) Transient response at t = 1, 2, and 4 in arbitrary units. The three dimensional plots show concentration $P(\vec{r}, t)$ (or C in the figure) as a function of x and y dimensions. The plots are superimposed over a contour plot of concentration to simplify visualization. The anisotropic diffusion tensor used had a 3:1 ratio of eigenvalues.

in biological tissue, but is usually a good approximation for a single fiber population.

2.2.2 Impermeable boundary conditions

Finite boundary conditions make the solution to a delta function much more difficult. Only impermeable boundary conditions are considered. Finite boundary conditions look at diffusion occurring within boundaries. An assumption is made now that diffusion is isotropic (i.e. **D** becomes a scalar), and that diffusion anisotropy comes from

a sampling of boundaries. In this section we will only consider a one dimensional wall boundary condition, for which an analytic solution is possible. Chapter 4 considers more complex boundary conditions through finite element simulation.

For isotropic diffusion from a delta function initial condition between a one dimensional wall, a series solution to (2.10) is available.

$$P(\vec{r}, t) = 1 + 2 \sum_n \exp\left(\frac{-n^2 \pi^2 D t}{|\vec{a}|^2}\right) \cos(n\pi \vec{r} \cdot \vec{a}^{-1}) \cos(n\pi \vec{r} \cdot \vec{a}^{-1}), \qquad (2.13)$$

where $\vec{a}$ is the one dimensional boundary condition, $\vec{a}^{-1}$ is the inverse of each of the components of $\vec{a}$ individually, and D is the isotropic diffusion coefficient. Figures 2-3(b-d) show the transient response for this solution. This solution is similar to a single fiber population in biology. The relationship between this solution and the anisotropic diffusion tensor is shown qualitatively by there relationships between Figures 2-2 and 2-3, namely that is that diffusion is greater in a maximal direction, and minimal in an orthogonal direction. This qualitative agreement justifies the use of a second order diffusion tensor assumption for simple boundary conditions such as a single fiber populations, but has limited relevance in more complex conditions, such as multiple fiber populations. Thus the most general representation of the diffusion data that is available is to know $P(\vec{r}, t)$ for all $\vec{r}$ and t and not make any assumptions about the underlying diffusion process and boundary conditions.

2.3   Diffusion in NMR

Torrey modified the Bloch equations (2.9) to account for diffusion, and thus created the Bloch-Torrey equations [42]. Stejskal further modified these equations to account for general anisotropic diffusion and velocity due to the diffusion equation (2.10) [38].

$$\frac{d\vec{M}}{dt} = \gamma \vec{M} \times \vec{B}_{ext} + \frac{1}{T_1}(M_0 - M_z)\hat{z} - \frac{1}{T_2}\vec{M}_\perp - \nabla \cdot \vec{v}|\vec{M}| + \mathbf{D}\nabla^2 \vec{M} \qquad (2.14)$$
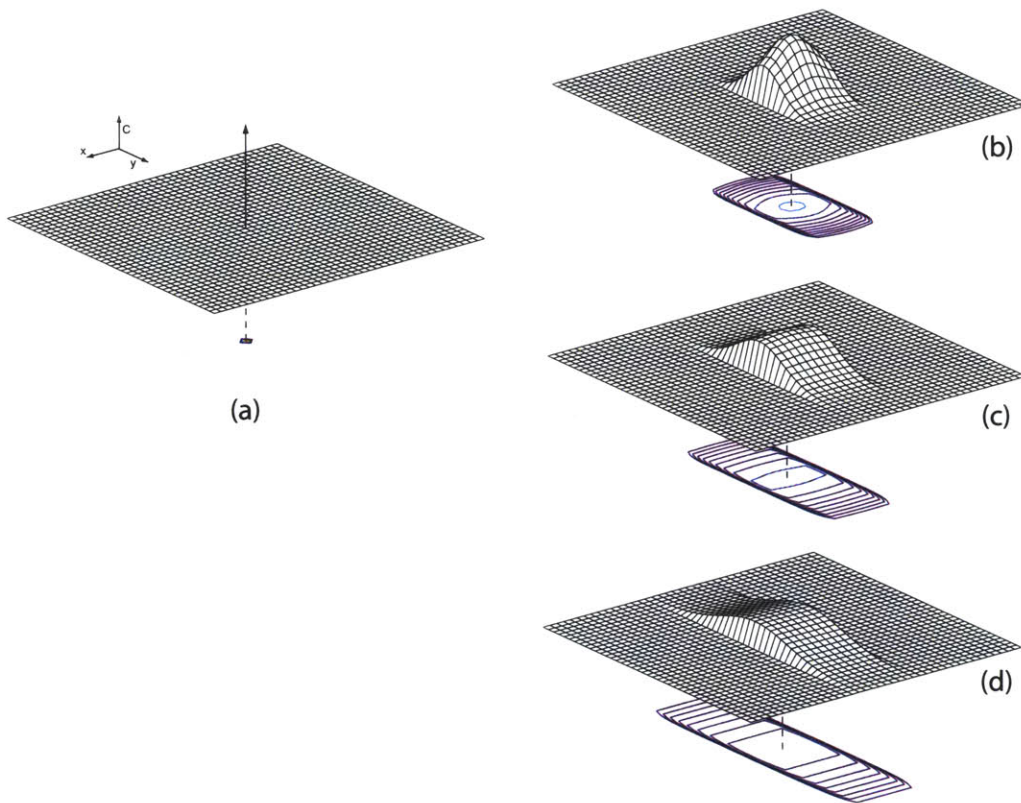
Figure 2-3: Two dimensional diffusion equation solution, with one dimensional bounded. (a) The initial point delta function in concentration. (b-d) Transient response at t = 1, 2, and 4 in arbitrary units. The three dimensional plots show concentration $P(\vec{r}, t)$ (or C in the figure) as a function of x and y dimensions. The plots are superimposed over a contour plot of concentration to simplify visualization. The one dimensional wall boundary condition becomes clear as diffusion time increases.

and again decomposing into two coupled ordinary differential equations and in a rotating coordinate frame, similar to equation (2.9)

$$
\begin{aligned}
\frac{M_{+'}}{dt} &= (\vec{\omega}_{1_{x'}} + i\vec{\omega}_{1_{y'}})M_z - i\Delta\omega M_{+'} + M_{+'}(|\mathbf{D}\nabla^2\vec{M}| - \nabla \cdot \vec{v}|\vec{M}| - \frac{1}{T_2}) \\
\frac{M_z}{dt} &= -|\vec{\omega}_1||M_{+'}| + \frac{M_0 - M_z}{T_1}
\end{aligned}
\tag{2.15}
$$

Equation (2.15) shows that diffusion terms attenuate the signal, similar to T_2, and velocity terms produce a coherent phase shift.

2.3.1 Pulse sequences

Finally we consider an actual scanning pulse sequence, which is NMR terminology for a time dependent series of magnetic field gradients in different spatial directions. The pulse sequence acts on the spin equations of motion and thus the response rf signal produced. This enables the interrogation of internal variables of the system, such as $\mathbf{D}$. The principal of using NMR to investigate the isotropic diffusion coefficient was first proposed by Stejskal and Tanner [39], using the spin echo method of Hahn [17], in an experiment that interestingly predates MRI[1]. Stejskal and Tanner solved the Bloch equations for this specific pulse sequence, called the pulsed gradient spin-echo (PGSE) sequence, and analytically found the magnitude of signal attenuation due to diffusion. The PGSE sequence is shown in Figure 2-4. The important feature of the PGSE sequence is that there is a diffusion weighting gradient of strength and direction $\vec{g}$ and duration δ, and is separated by the mixing time for diffusion to occur, Δ. The solution of equations (2.15) under the conditions of this pulse sequence is

$$
\begin{aligned}
M_{+'}(TE) &= M_{+_0'}(TE)\exp(-\gamma^2\delta^2\vec{g} \cdot \mathbf{D}\vec{g}\Delta - i\gamma\delta\vec{g} \cdot \vec{S}(\Delta)) \\
\vec{S}(t) &= \int_0^t \vec{v}dt'
\end{aligned}
\tag{2.16}
$$

---

[1] In practice we use a much faster acquisition than the spin-echo method called echo planar imaging (EPI). The fundamental concepts in terms of diffusion are the same for spin-echo and EPI.

where TE is the echo time and $M_{+'_0}(TE)$ is the signal at TE with no diffusion weighting. M_z is ignored because it is assumed that $T_1 \gg T_2$. By plotting the natural log of $M_{+'}$ against $|\vec{g}|^2$, Stetskal and Tanner confirmed the expected linear relationship in the isotropic, infinite boundary condition case. Then, because the velocity term is of little interest in our experiments, we seek to design the pulse sequence so to only be sensitive to diffusion and not velocity. This is accomplished with the double PGSE sequence shown in Figure 2-5. The results for the double PGSE sequence are very similar to the PGSE sequence, but due to the antisymmetry of the gradients, the coherent velocity is removed.

$$M_{+'}(TE) = M_{+'_0}(TE) \exp(-2\gamma^2\delta^2\vec{g} \cdot \mathbf{D}\vec{g}\Delta) \qquad (2.17)$$

One other feature of this sequence in the analysis of Stejskal and Tanner they considered δ to be infinitesimal in duration. However, experimentally this is not the case, and they defined an effective diffusion time Δ_e to account for finite pulse duration.

$$\Delta_e = \Delta - \frac{\delta}{3} \qquad (2.18)$$

These equations are good for analytically representing the data when the underlying diffusion process is given by equation 2.10 with infinite boundary conditions. Thus similar to the result in section 2.2.1, this result is only good for anisotropic Gaussian diffusion and not more complex boundary conditions.

To address the issue of complex boundary conditions, we consider diffusion as creating a probability distribution $P(\vec{r}, t)$ and look at the signal produced for an arbitrary probability distribution. Because of the constant velocity abolishment features of the double PGSE sequence, it is used in this further analysis. Considering, the probability distribution around a starting point to be a known quantity (see the results of sections 2.2.1 and 2.2.2), the solution to the Bloch equations (2.9) is available in a general form. For the signal for any general pulse sequence at time t, ignoring the attenuation affects of T_1 and T_2[2], the solution is written as a function of the proton

---
[2]This assumption is valid for when considering diffusion imaging because in quantitative diffusion
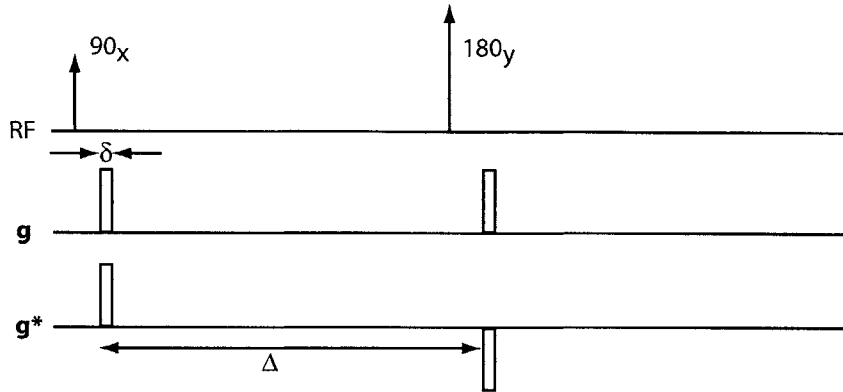
Figure 2-4: The pulsed gradient spin-echo (PGSE) sequence. The ordinate axis is time. The 90_x rf pulse is a $\vec{B}_1$ pulse that rotates magnetization from the z axis to the xy plane, rotating around the x axis. Subsequently, a diffusion weighting gradient $\vec{g}$ is applied for duration δ. This encodes a linear phase gradient across the sample. At some time before Δ, a 180_y pulse is applied. This reverse the direction of future diffusion weighting gradients, and can be thought of just applying a gradient sequence of $\vec{g}^*$. Then, due to the spin-echo effect, the signal reconverges at some echo time (TE) later [17]. However, this reconvergence of this signal is attenuated by random phase acquired due to diffusion, and is modified by coherent phase due to velocity.
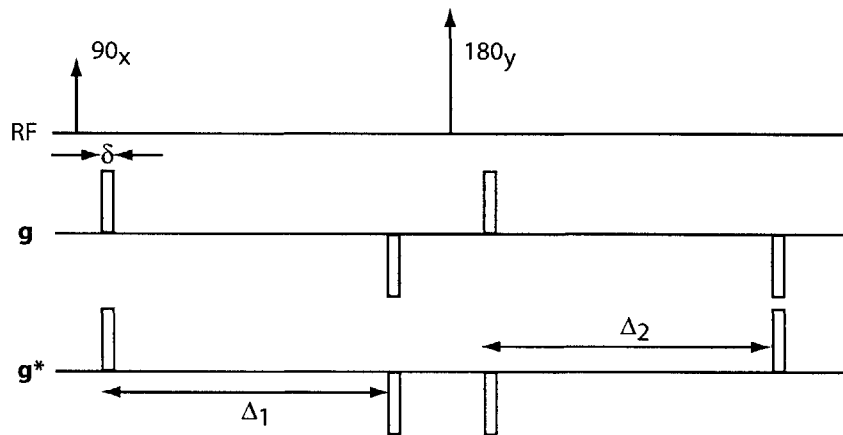

Figure 2-5: The double PGSE sequence is similar to the PGSE sequence shown in Figure 2-4, but contains an additional antisymmetric diffusion weighting sequence. This antisymmetry abolishes any coherent phase acquired by constant velocity. The effective diffusion time is doubled and equals 2Δ.

density $\rho(\vec{r})$.

$$M_{+'}(\vec{k}, t) = \int \rho(\vec{r}) \exp(i\vec{k} \cdot \vec{r}) d\vec{r}$$
$$k = \gamma \int_0^t \vec{g}(t') dt' \tag{2.19}$$

This equation forms the basis for normal structural imaging of biological tissue and is called k-space imaging. Then, substituting in the effect that the probability distribution $P(\vec{r}, t)$ has on the proton density,

$$\vec{M}_{+'}(\vec{q}, t) = \iint \rho(\vec{r}) P(\vec{R} \,|\, \vec{r}, t) \exp(i\vec{q} \cdot \vec{R}) d\vec{r} d\vec{R}$$
$$\vec{q} = \gamma \int_0^t \vec{g}(t') dt' \tag{2.20}$$

where $\vec{R}$ is the vector away from a starting point $\vec{r}$, and thus $P_s(\vec{R} \,|\, \vec{r}, t)$ is probability of diffusion to a distance $\vec{R}$ away from $\vec{r}$. The new variable $\vec{q}$ is defined to simplify representation. Then, an averaged probability distribution is defined over all starting points $\vec{r}$,

$$\bar{P}(\vec{R}, t) = \int \rho(\vec{r}) P(\vec{R} \,|\, \vec{r}) d\vec{r} \tag{2.21}$$

Substituting this definition and considering the double PGSE sequence, the equation is put into a final simplified form.

$$M_{+'}(\vec{q}, \Delta) = \int \bar{P}(\vec{R}, \Delta) \exp(i\vec{q} \cdot \vec{R}) d\vec{R} \tag{2.22}$$

This final form has the property that the probability distribution is the Fourier transform of the signal acquired in "q-space." This equation forms the basis for the more complex signal acquisition and processing methods described in Chapter 3.

---

imaging at least two images are necessary; one is a zero diffusion weighted image and the other(s) are diffusion weighted. The amount of signal attenuation is found by subtracting these two images

Chapter 3

Diffusion Imaging Methodology

Diffusion imaging in MRI has historically moved towards increased complexity and larger data sets. Initially, Taylor and Bushell realized that diffusion imaging could provide contrast concerning restricted versus free diffusions spaces in biological tissue [41]. Using diffusion to provide contrast in this manner has been proven as an excellent mechanism in the forewarning of stroke [27]. In this case, diffusion weighting is viewed either from a single direction, or with an isotropic measure (explained later as trace ADC). Even in these early experiments, researchers realized that the assumption of isotropic diffusion was not valid in most biological tissue. Basser proposed that diffusion in biological tissue could better be approximated as a second order tensor and provided a systematic processing scheme [6]. This view of diffusion requires at least six diffusion weighting directions, and provides the ability to discern a single orientation and related anisotropy through an invariant scalar fractional anisotropy (FA) measure. However in practice it was found that resolving a single orientation was not sufficient to determine orientation when multiple fiber orientation directions were present in a voxel. Thus, a number of high angular resolution diffusion (HARD) techniques have been proposed that collect data in many diffusion weighting directions. Such techniques include q-ball [43], diffusion spectrum imaging (DSI) [45], and higher order tensor (HOT) [22]. There is then a further post-processing method to aid in visualization of these complex data sets, called tractography. Tractography uses a volume data acquisition and connects the intervoxel fiber orientations. This chapter

will first discuss DTI and its invariant scalar measures, then DSI, then presents a brief description of tractography, and ends with the experimental methods used on the MRI scanner.

3.1 Diffusion tensor imaging (DTI)

Diffusion weighted images may be acquired with diffusion weighting gradients applied in any direction and magnitude. Assuming that diffusion conforms to an anisotropic Gaussian, then a second order diffusion tensor in the diffusion equation (2.10) suffices in describing the microstructure present in a voxel. Basser later showed this to be true for small diffusion times or large diffusion distances (although we believe the latter case is flawed due the high improbablity of long diffusion distances) [5]. The signal received will be attenuated by diffusion weighting with respect to a zero diffusion weighted image (called a b_0 image) precisely as given by equation (2.17). By taking the natural log of this equation, we get a linear equation of the diffusion tensor $\mathbf{D}$.

$$\ln(M_{+\prime}) = \ln(M_{+_0}) - \vec{q} \otimes \vec{q} : \mathbf{D}$$
$$\vec{q} = \gamma \delta \vec{g} \tag{3.1}$$

For any number of $\vec{q}$ values greater than six, a linear least squares solution is available for this problem. For this reason, Basser defines a "B" matrix, in which the least squares solution becomes:

$$\vec{d} = \left(\mathbf{B}^T \Sigma^{-1} \mathbf{B}\right)^{-1} \mathbf{B}^T \Sigma^{-1} \ln(M_{+\prime})$$

$$\mathbf{B} = \begin{bmatrix} q_1^1 q_1^1 & 2q_1^1 q_2^1 & 2q_1^1 q_3^1 & q_2^1 q_2^1 & 2q_2^1 q_3^1 & q_3^1 q_3^1 & 1 \\ q_1^2 q_1^2 & 2q_1^2 q_2^2 & 2q_1^2 q_3^2 & q_2^2 q_2^2 & 2q_2^2 q_3^2 & q_3^2 q_3^2 & 1 \\ & & & \vdots & & & \\ q_1^n q_1^n & 2q_1^n q_2^n & 2q_1^n q_3^n & q_2^n q_2^n & 2q_2^n q_3^n & q_3^n q_3^n & 1 \end{bmatrix} \Delta \tag{3.2}$$

$$\vec{d} = \begin{bmatrix} D_{11} & D_{12} & D_{13} & D_{22} & D_{23} & D_{33} \end{bmatrix}'$$

where q_i^j are the components of $\vec{q}$ for image j, D_{ij} are the components of $\mathbf{D}$, and

Σ is a noise covariance matrix associated with the nonlinear operation ln. Another useful variable that comes from this analysis is the b-value, whose components are given by $b_i = q_i^2 \Delta$; the b-value has inverse units of diffusion ($\frac{s}{mm^2}$), and in general is a good representation of the overall diffusion weighting in a certain direction.

This method produces a diffusion tensor for each voxel in of each MRI image, which may be many separate images for each slice of the structure. There are several methods of post-processing for diffusion tensor data that allow and simplify visualization of the data. The most complete method to view tensor data is visualized in terms of a three-dimensional shape that correlates to the relative directions and magnitudes of the diffusion tensor, that is its eigenvectors and eigenvalues respectively. Figure 3-1 shows an example of this representation for a 2D second order tensor. The diffusion tensor can also be visualized in terms of its scalar invariants. Two such often used invariants are the trace apparent diffusion coefficient (trace ADC), which is just the trace of the diffusion tensor, ands its fractional anisotropy (FA) which is given by

$$\text{FA} = \sqrt{\frac{3}{2}\frac{\Sigma_i(\lambda_i - \bar{\lambda}_i)^2}{\Sigma_i\lambda_i^2}} \tag{3.3}$$

where λ_i are the eigenvalues and $(\bar{\ })$ denotes the average.

The octahedral representation of diffusion tensors from MRI data of the cow tongue are given in the Results chapter 5 in Figures 5-1 and 5-2.

3.2 Diffusion spectrum imaging (DSI)

Since DTI assumed an anisotropic Gaussian model for diffusion and used a limited acquisiton in q-space, there was an interest in imaging increased complexity, that is imaging the probability distribution function for diffusion directly. Prior to the advent of DTI it was known that the probability distribution for diffusion could be imaged directly in q-space as given by equation (2.22) [10,11]. Q-space imaging did not reach the biological imaging world until after DTI, when researchers discovered its inability resolve crossing fibers in a voxel [15,30,44]. In order to achieve practical q-space imag-

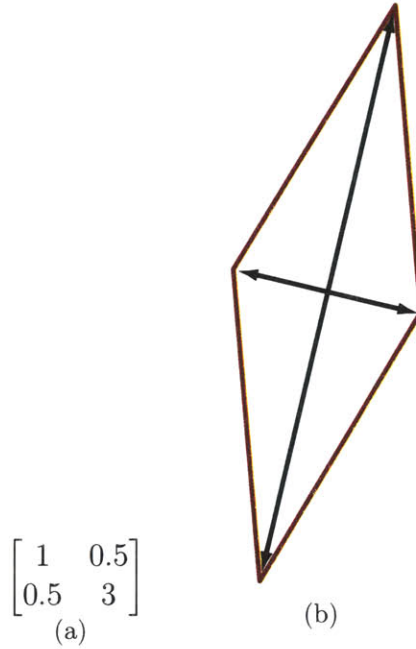$$\begin{bmatrix} 1 & 0.5 \\ 0.5 & 3 \end{bmatrix}$$

(a)

(b)

Figure 3-1: An arbitrary symmetric, positive definite tensor (a) was chosen to simulate an octahedral representation of eigenvalues and eigenvectors (b). The eigenvalues are $\{0.88, 3.12\}$ and the eigenvectors are $\{[-.97, .22], [.22, .97]\}$, which are orthogonal as expected. The trace ADC for this tensor is 4 and the fractional anisotropy measure is 4.76.

ing, DSI modifies the pulse sequence to include non-infinitesimal pulse width [21]. In this case the probability distribution imaged is not precisely the probability distribution function, but is the center-of-mass (COM) diffusion propagator [25]. However, in this thesis we use the term probability distribution function (PDF) to refer to the observed distribution obtained from DSI processing of the signal. The actual distribution differs from the this observed PDF due to the center-of-mass effects, scanning contrast, partial volume effects, sampling artifacts, and noise. However, none of these effects cause a mis-registration of maximum diffusion directions and thus we refer to the observed PDF as the PDF.

In DSI, the signal $M_{+'}(\vec{q}, \Delta)$ is acquired for a sphere of $\vec{q}$ vectors with indexed values in a Cartesian grid in q-space, in order to produce a three dimensional probability distribution. The PDF ($\bar{P}(\vec{R}, \Delta)$) is just the inverse Fourier transform of equation (2.22).

$$\bar{P}(\vec{R}, \Delta) = \mathcal{F}^{-1}\left[M_{+'}(\vec{q}, \Delta)\right] \tag{3.4}$$

44

where $\mathcal{F}^{-1}$ denotes the inverse Fourier transform. Similar to imaging in k-space[1], the spacing between $\vec{q}$ vectors defines the field of view and the maximum $\vec{q}$ vector defines the resolution of the PDF. The values of $M_{+'}(\vec{q}, \Delta)$ are placed in a matrix with indices given by the indices of the $\vec{q}$ vectors, and the 3D inverse Fourier transform is computed. The 3D PDF represents a spatial volume and it is necessary to reduce it in dimensions to make visualization more clear. The method typically employed in DSI is to integrate weighted radially by the magnitude of $\vec{R}$:

$$\text{ODF}(\hat{u}, \Delta) = \int \bar{P}(\rho\hat{u}, \Delta)\rho\hat{u}d\rho \tag{3.5}$$

where $\hat{u}$ is a unit vector in the direction of $\vec{R}$. This produces a probability distribution that is a function only of fiber angle and is weighted to better show long diffusion distances. This new data set is termed the orientational distribution function (ODF) and provides a probability distribution for diffusion for a set angular direction, regardless of the magnitude of the diffusion. To further simplify visualization, the ODF is normalized by subtracting the smallest magnitude value from the entire distribution. The ODF is then plotted with colors corresponding to direction and magnitude, and radii are defined by the values of the ODF. Q-space and k-space imaging are combined by taking a k-space image for each point in q-space, thus resulting in a separate diffusion propagator result for each voxel in the k-space image.

The resulting ODFs for the bovine tongue and esophagus are given in the Results chapter 5 in Figures 5-1 – 5-5 and 5-11.

3.3   Tractography

Each voxel in a DTI data set has one primary eigenvalue, and associated eigenvector direction, which defines a 3D vector for each voxel in the 3D set of images. Thus there is a 3D vector field. Connecting vector along the directions in vector fields is not a new concept, and is called constructing streamlines. Mathematically a streamline is

---

[1]k-space is normal MRI image acquisition, in which $\rho(\vec{r}) = \mathcal{F}^{-1}\left[M_{+'}(\vec{k}, t)\right]$

defined as the solution of an ordinary differential equation

$$\frac{d\vec{S}(s)}{ds} = \vec{v}(\vec{S}(s))$$

(3.6)

where $\vec{S}(s)$ is the streamline, s is a path coordinate along $\vec{S}$, and $\vec{v}$ is the vector field. Equation (3.6) in words, defines that the streamline will be tangent to the vector field at all points. Generating streamlines corresponding to a vector field in biological data has been termed tractography [4]. Tractography applied in the brain is believed to correlate to neural connectivity, and in muscle tissue, we believe it correlates to myoarchitecture.

A DSI data set will have one or more 3D vectors for each voxel, each vector relating to a local maxima of the ODF. In this case we use generalized streamline tractography [43]. Generalized streamline tractography operates by adding a constraint to the streamlines that for intervoxel connectivity a certain angular threshold must be met. If the threshold is not met, then the tract will stop. Also, if a tract happens upon a voxel with two or more vectors that meet the angular threshold criteria, then the tract will continue along the vector of least angular difference with itself.

The results for tractography of both the bovine tongue and esophagus are given in the Results chapter 5 in Figures 5-6 – 5-9 and 5-12.

3.4   MRI protocol

For imaging the bovine tongue and esophagus, diffusion weighted imaging was applied to the entire tissue and was assesed using both DTI, DSI, and DSI tractography. Magnetic resonance imaging was performed on 4 ex-vivo cow tongues, 4 ex-vivo cow esophagi, and 2 ex-vivo pig esophagi, obtained from Blood Farms (West Groton, MA). Whole specimens were refrigerated and scanned within 24 hours of harvest. Data was acquired with a clinical scanner (Siemens Allegra 3T) for the tongues and with both a clinical and small-bore animal scanner (Bruker Biospin 4.7T) for the esophagi.

The imaging protocol employed a diffusion gradient sampling scheme, which con-

sisted of a key-hole Cartesian acquisition to include q-space values lying on a Cartesian grid within a sphere of radius $|\vec{q}_{max}|$, for a total of 515 sampling points. The imaging experiments are summarized in Table 3.1

Table 3.1: MRI scanning protocol.

	4 cow tongues	2 cow esophagi	2 cow esophagi, 2 pig esophagi
Scanner	Allegra 3T	Allegra 3T	Bruker 4.7T
$|\vec{b}|$	5500-8500 $\frac{s}{mm^2}$	5500-8500 $\frac{s}{mm^2}$	14,000 $\frac{s}{mm^2}$
δ	not available[2]	n/a	9.5 ms
Δ	n/a	n/a	19 ms
$|\vec{g}|$	30 mT/m	30 mT/m	380 mT/m

Chapter 4

Validation of Diffusion Imaging Techniques

The statistically averaged diffusion environment within intact skeletal muscle tissue is largely unknown by methods other than MRI diffusion imaging[1]. Since MRI diffusion imaging is subject to many experimental conditions that are not part of the simple model for anticipated diffusion attenuation, we found it necessary to perform validation with simple structures. These simple structures are reminiscent of skeletal muscle tissue, but have a precise quantifiable structure and thus a calculable diffusion environment. The validation was performed with both a finite element computer model and a physical microfluidic model. The finite element model provided a simulation of the "ideal" diffusion imaging pulse sequence, as well as a physically realizable one. The microfluidic model was scanned experimentally with an MRI diffusion imaging sequence.

In order to construct models for diffusion, first the biological diffusion environment is considered. Skeletal muscle tissue is composed of directional bundles of muscle fibers. The muscle fibers are shown in relation to the overall muscle tissue in Figure 4-1. The average 3D microstructure of these muscle fibers is relatively simple. The microstructure is viewed as aligned, intracellular fluid filled cylinders surrounded by

---

[1]Classical histology and two photon microscopy are two other methods for viewing microstructure, but neither is directly related to water environment only, as MRI is.

extracellular fluid. Thus, to abstractly represent muscle tissue within a voxel only requires an orientational vector. However, this simple microstructure leads to a complex multi-compartmented diffusion environment that is not easily solved analytically or simulated. Despite this complexity, an adequate general rule for describing the diffusion environment has been that the muscle fiber bundles permit water molecules composing the intra- and extracellular fluid, to diffuse preferentially in the direction of the fiber bundles. Preferential diffusion is the basis of the diffusion signal in which a local maximum direction of anisotropic diffusion correlates directly to the direction of the fibers in that region. This validation will investigate the range of validity of this general rule for determining fiber direction.
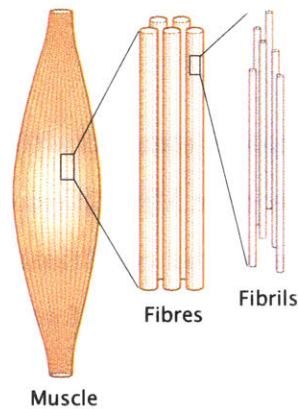

Figure 4-1: Illustration of muscle fiber scaling [46]. The resolution used in diffusion imaging is on the order of muscle fibers.

For the purposes of validation, only 2D shape models were developed due to the increased difficulty of 3D simulation and construction. For both simulation and experiment, simple two dimensional shapes were constructed that simulate of the microstructure boundaries found in biological muscle tissue. Additionally, the same shapes were used in both the microfluidic validation and the finite element analysis. This correlation provides a method for validating the computer model so that the computer model could later be used to evaluate more complex arrangements not possible with microfluidics[2].

---

[2]However, the experimental pulse sequence for microfluidic validation was flawed and no useable data was available in time for this thesis

The rest of the chapter is organized in two parts. First, the finite element model construction and simulated results are presented. Then the second section discusses microfluidic construction methods and experimental results.

4.1 Finite element analysis

The finite element method is a method for solving partial differential equations (PDEs) with complex initial and boundary conditions. The finite element solution is accomplished by breaking the shape of the boundary conditions (called the domain) down into smaller elements in a procedure called constructing the mesh. Figure 4-2(a) shows a a complex 2D shape with various boundary conditions meshed into smaller triangular elements. The PDE is then solved numerically on each element while maintaining continuity between adjacent elements. Most PDEs are not analytically solvable on complex domains such as the one in Figure 4-2(a), but the finite element method provides a reasonably close numerical solution. The accuracy of the solution is increased by simply making the mesh finer and/or changing the type of finite elements used. The solutions calculated for this project use a mesh similar in coarseness to that shown in Figure 4-2(a) and use the simplest type of 2D finite elements, namely linear triangular elements.

The type of PDE relevant to diffusion is a parabolic PDE with the general form

$$\frac{\partial P(\vec{r}, t)}{\partial t} = D\nabla^2 P(\vec{r}, t), \tag{4.1}$$

where $P(\vec{r}, t)$ is the concentration of water at the location $\vec{r}$, and D is the scalar diffusion coefficient of water. This PDE is relevant for the transient behavior of diffusion transport and storage, but assumes that the velocity term in the more complete equation (2.10) is zero. In order to solve this PDE using finite elements, it first is converted from its current form (called the strong form) to a weak form. The weak form has a lower order continuity constraint for the derivatives of $P(\vec{r}, t)$ than the strong form, allowing discontinuities between the elements, which allows for a non-

exact, best estimate, numerical solution. The weak form, derived by applying the divergence theorem to the strong form, is:

$$\int_\Omega (\nabla \cdot w)(D\nabla P(\vec{r}, t))d\Omega - w\frac{\partial P(\vec{r}, t)}{\partial t} = 0. \tag{4.2}$$

In the weak form, w is an arbitrary weighting function with the same form as the finite element and Ω is the domain. The weak form is further modified to a numerical summation approximation, thus making solution possible on piecewise triangular elements as shown:

$$\sum_{e=1}^{n_{el}} \left[\int_{\Omega^e} (\nabla \cdot w^e)(D^e\nabla P^e(\vec{r}, t))d\Omega - w\frac{\partial P^e(\vec{r}, t)}{\partial t} \right] = 0. \tag{4.3}$$

where the superscript e denotes the association with element and n_{el} is the number of elements.

Thus, the PDE is solved by breaking any complex 2D shape and boundary conditions into a mesh of smaller triangular elements, for which a piecewise element approximation can be solved. The parabolic PDE solved is this report is the diffusion equation (4.1), used exclusively with zero flux Neumann boundary conditions and delta function initial conditions.

4.1.1 Averaged probablity distribution function for diffusion

Fluid molecules are constantly in a state of motion, even when the fluid appears at rest on a macroscopic scale. This random motion of molecules is called diffusion, and in the case of diffusion occurring within a homogeneous medium such as pure water, the motion is called self-diffusion. A common example of diffusion is the motion that is seen when a droplet of dye is dropped into a glass of water. The dye makes the diffusion process visible, but diffusive motion is occurring all the time, as is the case for self-diffusion in glass of pure water. This concept is similar to running the water dye experiment many times with the dye droplet at many different starting positions in the glass. NMR diffusion imaging inherently provides a method

to track the diffusion occurring around each starting point, summed over all starting points within a volume. Self-diffusion is simulated with the finite element method by capturing the diffusion associated as many different starting points in the shape as computationally possible.

The relevant dye droplet analogy in the discretized finite element analysis is to have a delta function at each mesh point and run the simulation many times for each point in the mesh. The resulting self-diffusion dataset provides the spatial values of water concentration for several time steps as the water diffuses around the delta function. The delta function provides the initial condition for the simulation and the boundary conditions are provided be the 2D domain of the simulation. In all simulations, the boundary conditions are zero flux Neumann conditions, which means that water is not able to permeate through the walls. The entire dataset is saved for subsequent diffusion imaging processing.

4.1.2   Simulation Processing

The complete data set is then processed into the format that would be obtained from an actual NMR diffusion imaging scan. This format is obtained by applying simulated, time dependent, directional diffusion gradients in the same way as would occur during an scan. The gradients produce a spatially dependent phase change for each mesh point in the 2D shape. The signal magnitude at the mesh point is proportional to concentration at that mesh point. Thus each mesh point has a phase and a signal magnitude associated with it for each gradient applied. This mesh point data signal magnitude and phase is calculated for several different diffusion gradient magnitudes and directions, similar to the gradients applied in an actual scan. The results for all of the different simulations are summed together, as would occur during an actual scan of self-diffusion.

Post processing of the data set is performed with the same algorithms as the processing of experimental data. The different types of post processing applied are DTI and DSI, for which complete descriptions are provided in chapter 3.

4.1.3 Simulation Results

Several shapes were simulated with the finite element analysis method and post processed with the methods described in this thesis. The step by step results of data processing are presented for a complex crossing fiber shape in Figure 4-2. The crossing rectangles are a model for the crossing muscle fibers, typically seen in the core of the tongue. This figure shows that maxima of the probability distribution function align with primary fiber directions. The results are similar when a realistic simulated scanning sequence for DSI is applied, but the maxima become more pronounced due to the COM formalism discussed in section 3.2. As expected, the diffusion tensor approximation is not able to well describe the crossing fiber case. This validates the ability of the probability distribution function for diffusion to determine orientation of the underlying fibers of this simple model.

4.2 Microfluidic experiments

Experiments were performed in an MRI small bore animal scanner (Bruker Biospin 4.7T) with a defined microstructure in order to experimentally validate the ability of DSI to discern crossing fibers, and simply to compare with the results of simulation. Unfortunately the diffusion weighting scanning sequence was flawed and we were unable to obtain valid results. We had used a new, untested stimulated echo sequence because the amount of water in our microfluidic phantom was very small and we couldn't use the routine echo planar imaging (EPI) sequence. Thus we present the methods used in microfluidic construction and then some of the results, showing the problems with the scanning sequence.

4.2.1 Microfluidic construction methods

The phantoms were created using soft lithography, a relatively inexpensive and reproducible method for carrying out micro- and nano-fabrication. During soft lithography, a master slide is created with patterned relief structures. These structures
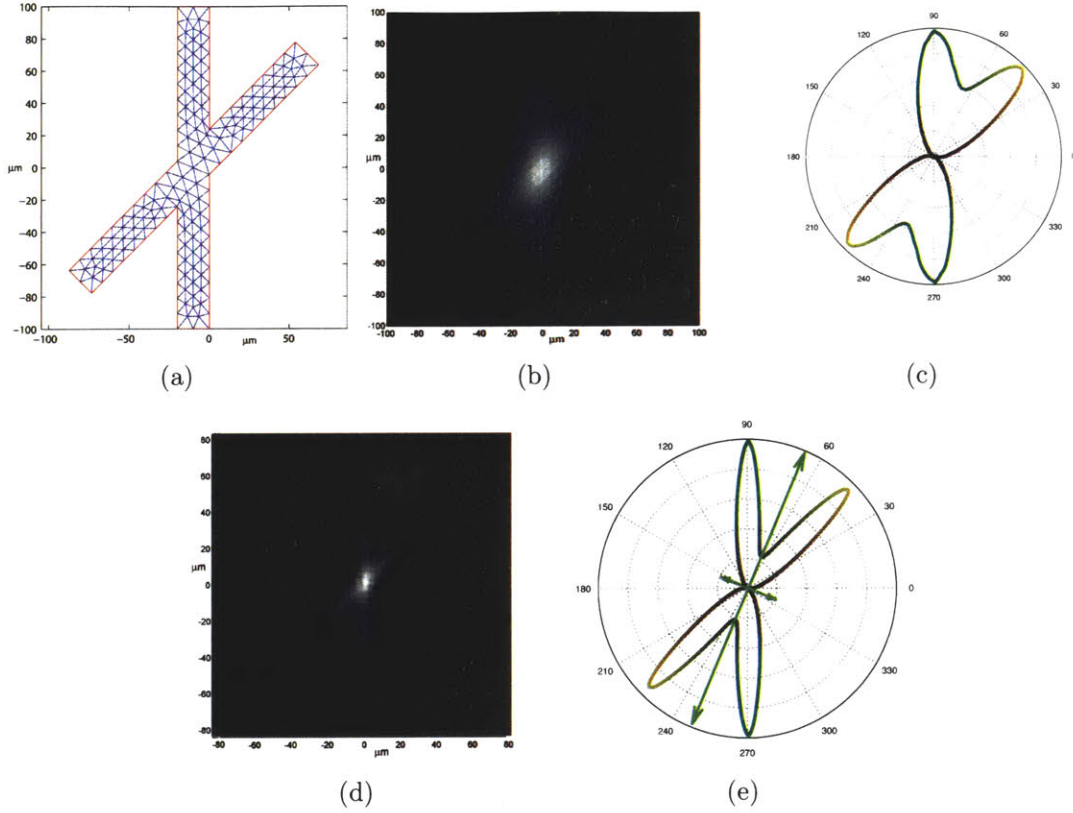
(a)　　　　　　　　　　　(b)　　　　　　　　　　　(c)

(d)　　　　　　　　　　　(e)

Figure 4-2: Finite element simulations were obtained in order to portray the behavior of the probability distribution function (PDF) for a simple set of two-dimensional crossing fibers with communicating water, employing water diffusion at $\Delta = 500\,ms$ and isotropic water diffusion coefficient $D = 2.5 \times 10^3\,\frac{\mu m^2}{s}$. (a) Automatically generated finite element mesh with 189 points depicting realistic geometry of size and angular relationship for crossing skeletal muscle fibers. (b) Image depicting the PDF computed from the simulation. (c) Radially weighted orientational distribution function (ODF) computed from the image in part (b). (d) Simulation of an actual DSI experiments employing the crossing fiber model shown in (a). A finite pulse-width PGSE sequence was simulated with $\delta = 350\,ms$, $\Delta = 600\,ms$, and a 10 mT/m maximum gradient strength. The resulting diffusion propagator obtained from the simulation is shown. This propagator is physically interpretable as the center of mass (COM) propagator. (e) Radially weighted ODF superimposed on the eigenvectors calculated from the simulation data using a DTI approach. The maximum DTI eigenvector is limited to bisecting the two simulated fibers.

create channels ranging from 30 - 100 μm. A polymer is then poured over this slide, cured, and then peeled off.

The master for these phantoms was created using a negative photoresist. During this process, photoresist is poured over a 3.5 in Si wafer (Silicon Quest, Santa Clara, CA). The unit is spun to create a thin, even film or a desired height and then baked until hard. Lithography masks (Mika color, CA) were designed and printed at 3550 dpi. They were placed over the hardened photoresist and then entire unit is exposed to UV light. Polymethylacetate (PMA) (Microchem, Newton, MA) was then used to remove all the unexposed photoresist. The remaining photoresist is the relief on the master slide. Finally, a polymer is poured over the master and baked. The hardened polymer is the microfluidic structure.

For this set of phantoms, the master slide reliefs were 100 μm wide, 100 μm tall, and 100 μm apart. The master was coated with poly(dimethylsiloxane) (PDMS) (Robert McKeown, Cambridge, MA). PDMS was chosen because of its numerous properties that make it very useful for soft lithography. PDMS comes in a two part kit: a liquid monomer and a curing or crosslinking agent. The two parts are mixed together at a ratio of 20:1 (monomer:crosslinking agent) and then poured onto the master and spun to create a thin layer. The master/polymer complex is baked to slightly harden the polymer. The process is repeated with another master slide, except the PDMS is poured on heavily to create a thick film. The thick polymer is cut from the master and then placed on top of the thin polymer layer. Finally, the complex is baked again. The final product is a bi-layer phantom.

4.2.2 Results

The q-space acquisition involved 515 points in q-space, filling a sphere on a Cartesian grid. Due to symmetry, the full 515 points are not really necessary; only half of q-space is really necessary, the symmetric half is the complex conjugate of the acquired half because the scanned image is real. Consequently, when viewed as magnitude

images, the two images with symmetric gradients should be almost exactly the same[3]. However, the full sphere in q-space is usually acquired because of the added signal to noise ratio it provides and the increased simplicity of processing. We ran scans with both single fiber populations and crossing fibers before noticing that there was an issue with the data collected. The issue was that the magnitude images acquired for symmetric gradients were vastly different when using the stimulated echo sequence (Figure 4-3). For comparison the symmetric gradient images are also shown for the EPI sequence with an esophagus in Figure 4-4. This points to a problem in the scanning pulse sequence, most likely that the imaging gradients were providing an unknown amount of diffusion weighting that was stronger than the applied diffusion weighting gradients. We learned that it is important to validate the scanning pulse sequence before using the scanner to validate DSI. One method for validating the pulse sequence is to observe that the magnitude images for symmetric gradients are about the same.

---

[3]The reason they might not be the same is because of noise and the center of q-space being slightly shifted due to imaging related gradients
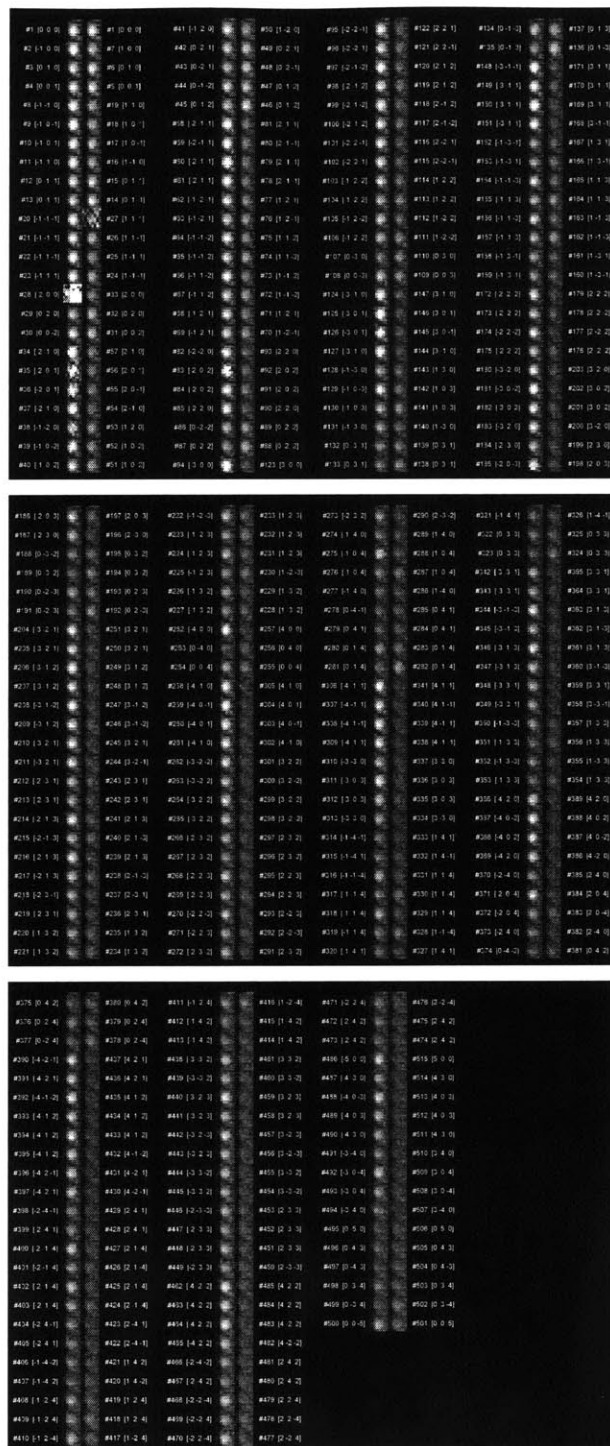
Figure 4-3: Results for scanning a crossing microfluidic phantom with a diffusion weighted stimulated echo sequence in 515 directions. Gradient number and direction is placed to the left or right of image. In addition to several poor scans (e.g. #25), there is a more fundamental problem that symmetric gradients directions do not have equal magnitude as they should.
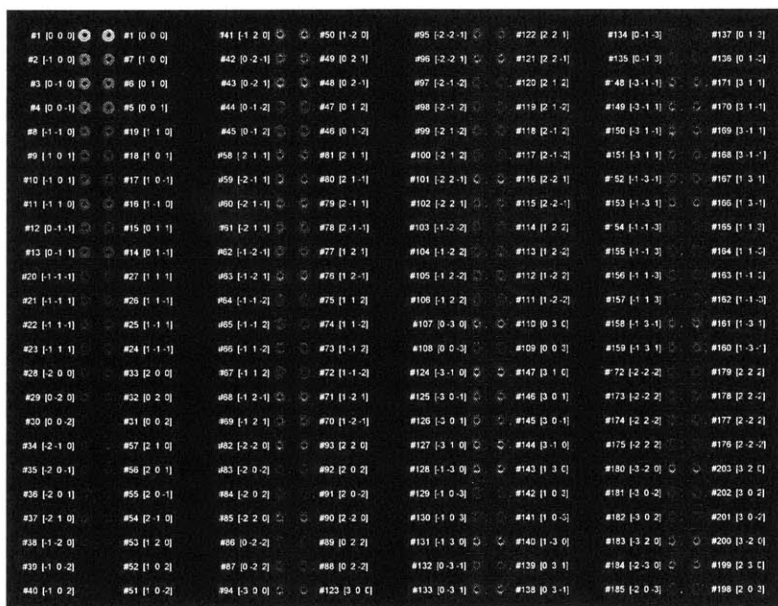
Figure 4-4: Results for scanning a cow esophagus with a diffusion weighted EPI sequence. Only the first 200 gradient directions are shown. In comparison with Figure 4-3, the results for symmetric diffusion weighting gradients are equal, as they should be.

Chapter 5

Results

Figures

The results section is largely image based, and as such, is organized beginning with a summary list of figures, followed by this small text summary, and then the figures are presented. All figures are representative of the multiple tissues scanned. First a comparison of DTI compared to DSI in the anterior tongue is shown in Figures

61

5-1 and 5-2, showing the superior angular resolution of DSI. Then multi-slice images of orientational distributions functions from the tongue data are shown in Figures 5-3 – 5-5. DSI tractography images of the tongue are shown in Figures 5-6 – 5-9. The bovine esophagus was also scanned, but was not further considered in this thesis other than the ODF images shown in Figure 5-11 and the tractography image of Figure 5-12.
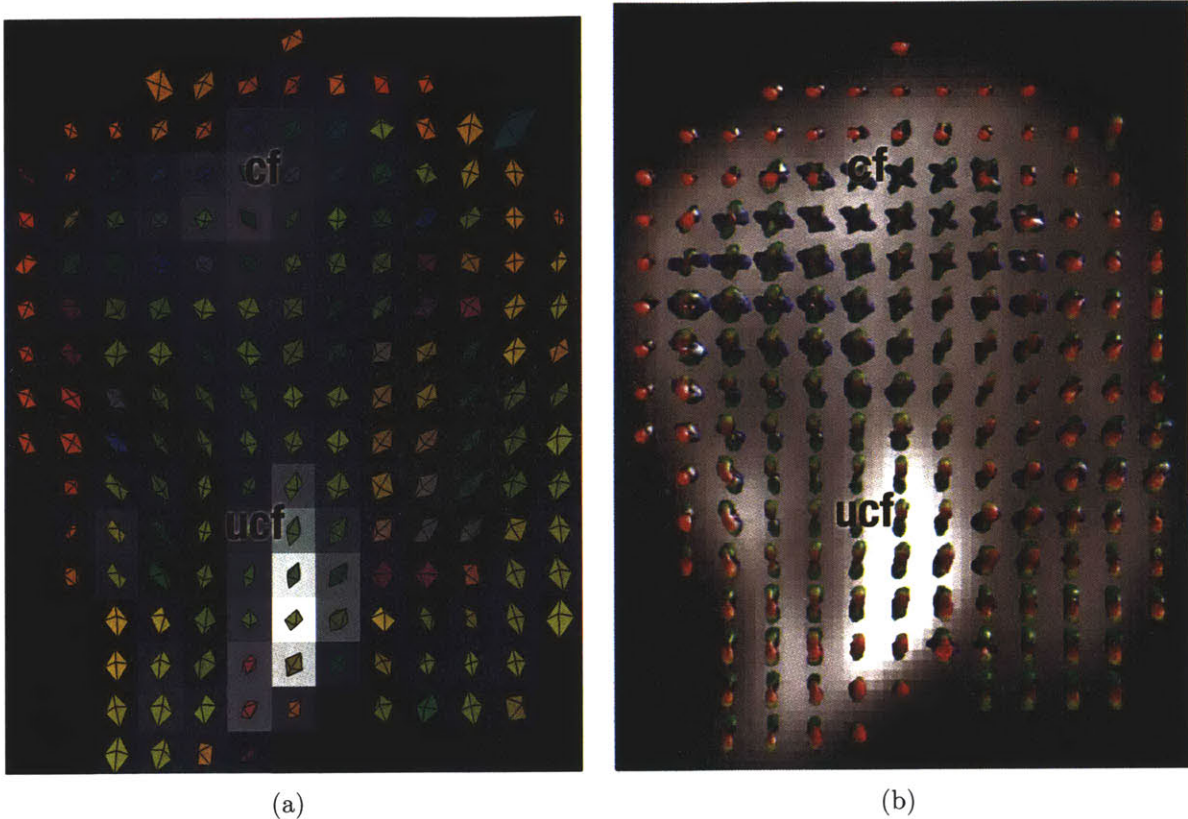
(a)   (b)

Figure 5-1: Shown are diffusion images obtained from an anterior axial slice in the intact and excised bovine tongue. DSI data were obtained using the pulse sequence herein for tissue specific q-space imaging. DTI constitutes a weighted least-squares solution of the Gaussian diffusion tensor model using the same dataset. The complete 3D diffusion tensor was computed for each voxel and visualized as octahedra, whose axes were scaled by the size of the eigenvalues and oriented along the corresponding eigenvectors in (a). The DSI dataset confirmed distinct fiber population heterogeneity in the anterior mammalian tongue, and in particular explicitly delineated orthogonally aligned crossing fiber populations (b). In contrast, the DTI dataset demonstrated a characteristic octahedron associated with a low anisotropy condition, consistent with equal populations of fibers in oblique directions to each other, but not designating an explicit angular relationship. The "ucf" and "cf" fibers represent uncrossed fibers and crossing fibers respectively, for which magnified views are shown in Figure 5-2. Color scheme is red-longitudinal/out of page, green-vertical, blue-transverse
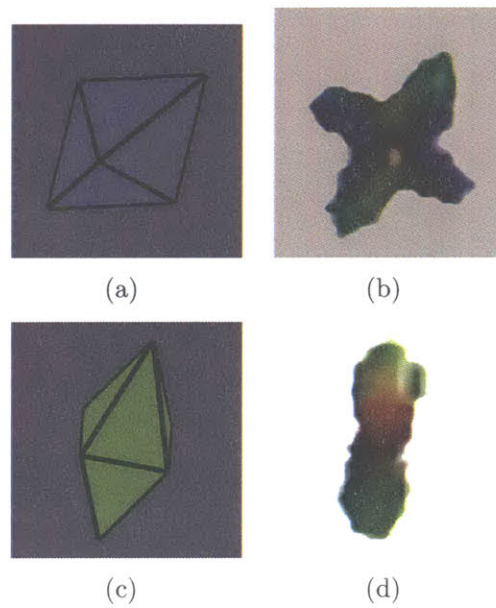
(a) (b)

(c) (d)

Figure 5-2: Zoomed images from Figure 5-1 (a) DTI representation of crossing fibers with little orientational specificity. (b) DSI orientational distribution function for the same voxel as (a) showing crossing fibers with clear angular relationships. (c) DTI representation of a single fiber population is adequate to determine fiber orientation. (d) DSI for same image voxel as (c) shows no improvement in fiber orientation resolution.
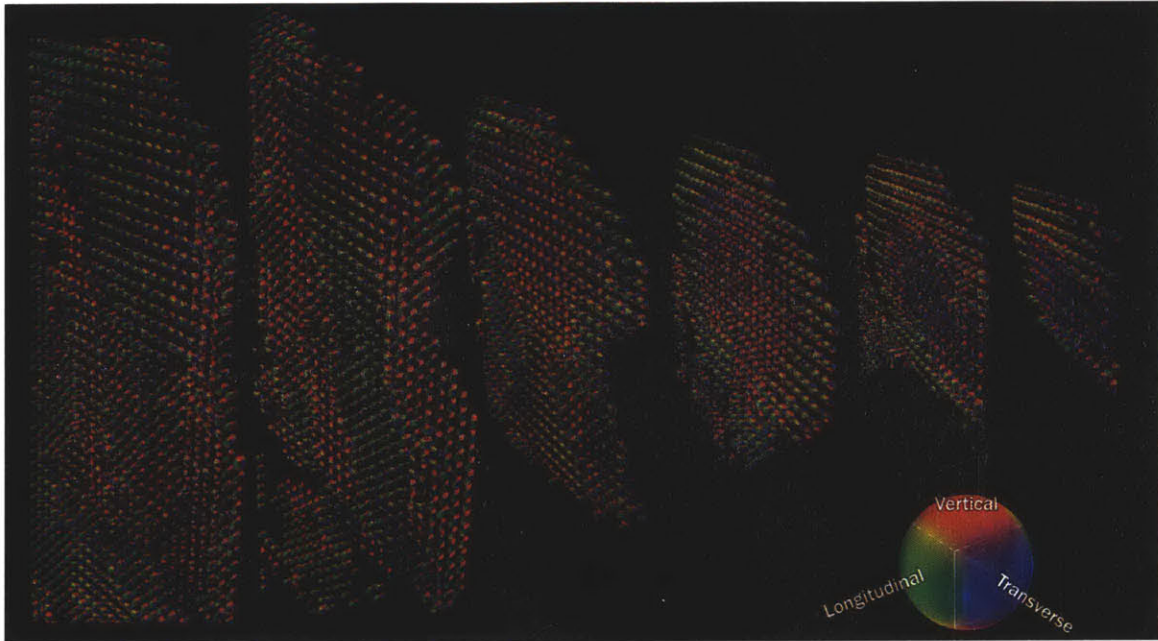
Figure 5-3: Sequence of axial slices depicting orientational distribution functions (ODFs) for each voxel from a multislice DSI acquisition of an ex-vivo bovine tongue. These slices are only a subset of the entire dataset, which is 64x64x25. There is clear correlation the the DTI axial slice data set (Figure 1-6) showing similar muscle fiber zones, by color coding. The color-code is shown in the color sphere (inset lower right). The sheath consisting of superior and inferior longitudinal muscles is green, corresponding to its longitudinal fiber orientation, and the tongue core is red and blue, corresponding respectively to horizontal and vertical crossing fiber orientations, whereas the extrinsic genioglossus(green-red) and hyoglossus (red-green) muscles are oblique.
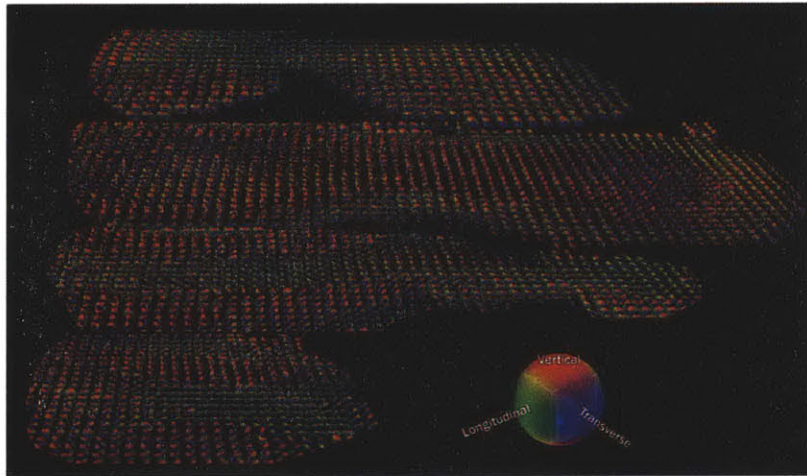
Figure 5-4: Sequence of four horizontal slices depicting ODFs for each voxel from a multislice DSI acquisition of an ex-vivo bovine tongue. These slices are only a subset of the entire dataset, which is 64x64x25. This image shows more prominently the superior (top slice) and inferior (third slice from top) in green corresponding to longitudinal fibers. The bottom slice shows the geniglossus fibers (green) and the two hyoglossus fiber populations (red).
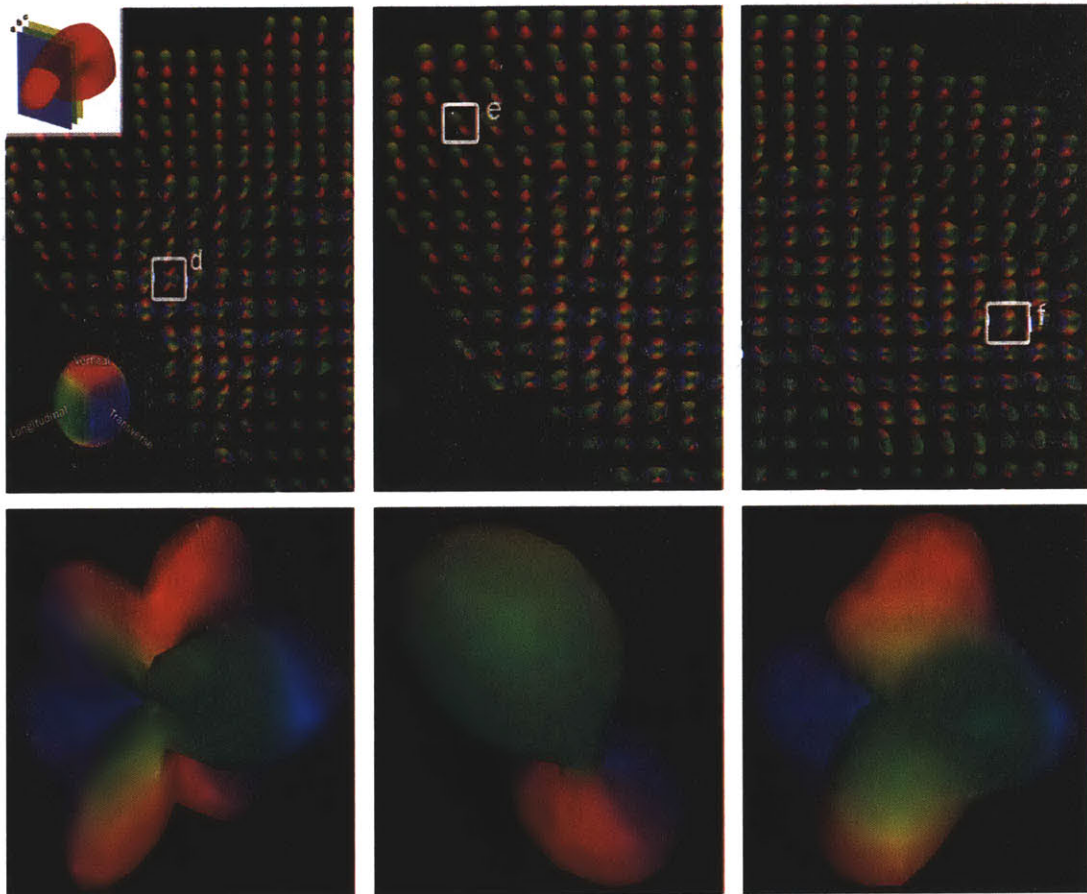
Figure 5-5: (a),(b), and (c) DSI image of ODFs in three adjacent axial slices in the anterior tongue. The color coding is red - vertical, blue - transverse, green - longitudinal. (a) and (b) show sections left of the midline, (c) is right of the midline. (d), (e), and (f) show selected regions with increased magnification to discern detail of the ODFs. (d) Voxel with at least three distinct crossing fiber populations. (e) Single population of longitudinal fibers oriented diagonally inward toward the tip of the tongue. (f) Voxel with two crossing fiber populations.
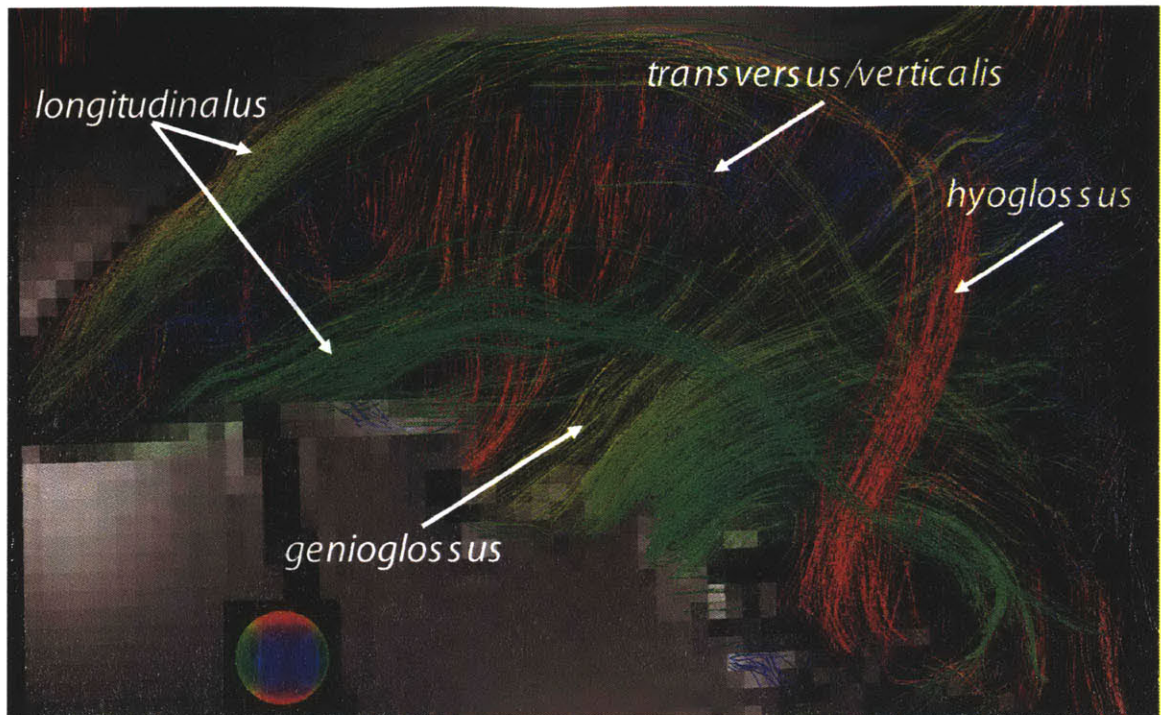
Figure 5-6: Tractography performed on tongue DSI data set. The tracts further simplify visualization and relevance of fiber populations. Tracts are colored by their starting point direction given by the inset color sphere. This is a sagittal slice of the tongue which shows only tracts passing through a mid-sagittal plane. The superior and inferior longitudinalis fibers (green) are shown sandwiching the core. Longitudinalis fibers actually surround the entire core transversely as well, but these fibers don't pass through the mid-sagittal plane. The genioglossus fibers fan radially and merge with the core fibers. The core fibers themselves cross vertically and transversely and thus are shown in red and blue. Last some of the hyoglossus fibers appear in this view as well because they have a midline posterior connection point to bone.
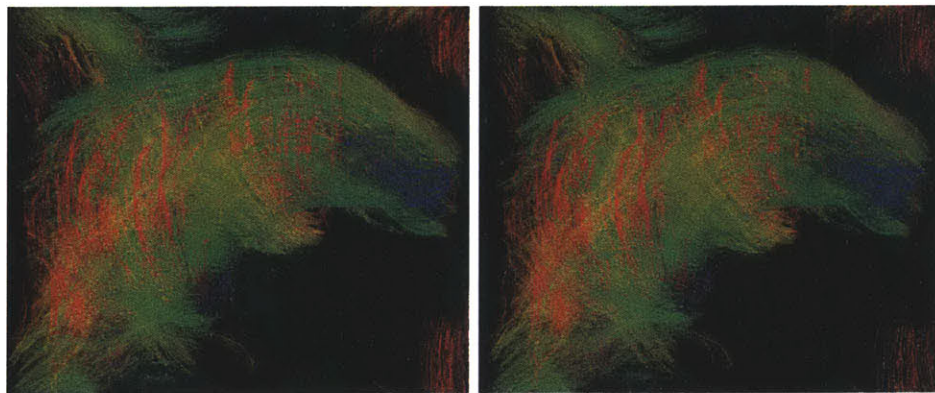

Figure 5-7: A stereo pair of all of the fibers from the tongue tractography data set. This may help is distinguishing 3D fiber relationships, and in visualizing the tongue as a whole. This is a sagittal view with the tip pointed right. Tracts seen surrounding the tongue are artifacts of magnetic field and/or gradient inhomogeneity.
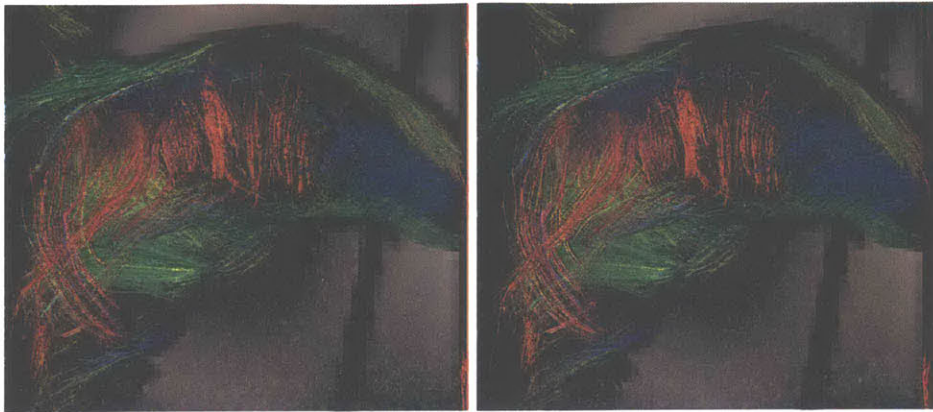
Figure 5-8: Another stereo pair of images showing only a mid-sagittal slice, similar to Figure 5-6. This image interestingly shows a greater prominence of transverse fibers of the core at tip (blue), while vertical fibers are more prominent in the middle (red).

Figure 5-9: An expanded view of the stereo pair in Figure 5-8 to discern increased detail.
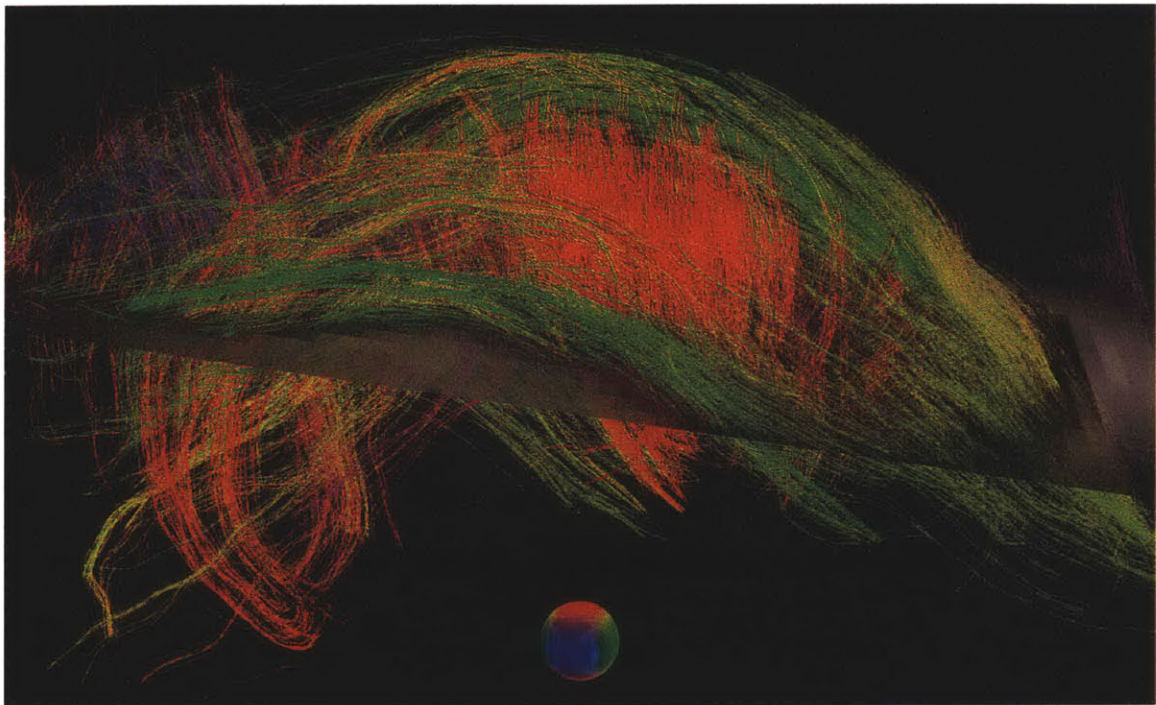
Figure 5-10: A sagittal view of the tongue showing only fibers crossing through a horizontal plane. This image shows the entire encapsulation of the core by the green longitudnalis fibers. The genioglossus fans posteriorly and vertically; vertically it merges with core verticalis fibers (center red).
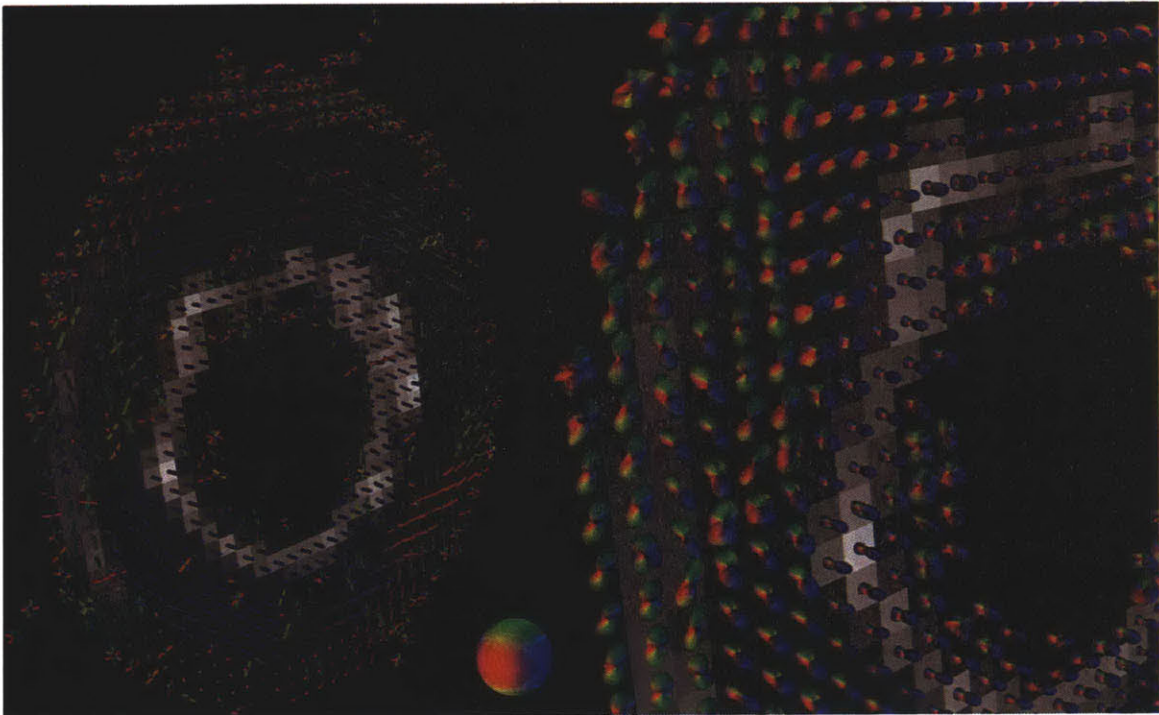
Figure 5-11: Axial slice of the bovine esophagus showing ODFs on the right and principle directions on the left. The principle directions are vectors associated with local maxima of the ODFs. An inner ring showing longitudinally oriented fibers corresponds to longitudinal fibers in the mucosa/submucosa. Precise orientations of the outer layers are difficult to discern in this image.

<div align="center">(a)</div>
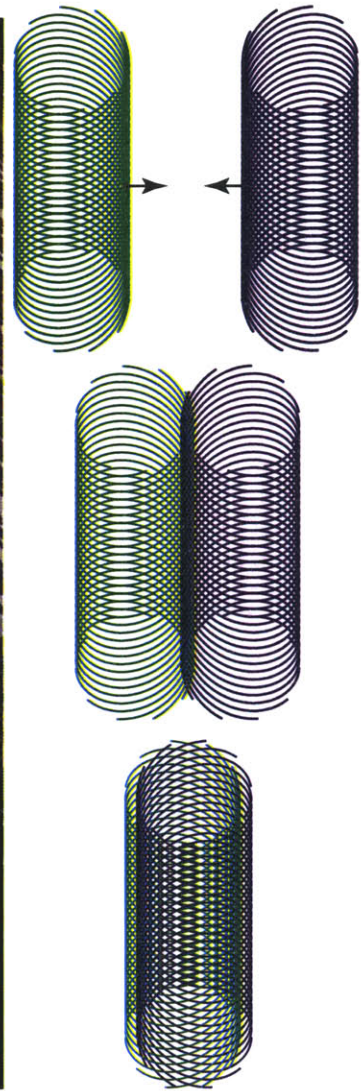
<div align="right">(b)</div>

Figure 5-12: (a) DSI tractography applied to the bovine esophagus shows two helical layers outside of the longitudinal layer. The helical layers have opposite helix angle and interdigitate along a longitudinal zone ("zipper"). (b) A schematic representation of two layers of opposite helix angle creating the structure see in the esophagus.

Chapter 6

Conclusions

The data acquired from the research of this thesis was largely successful in portraying 3D myoarchitecture of the tongue. Specifically, the DSI tractography images are shown as an excellent means for concisely displaying 3D myorachitecture, which correlates well with classical depictions of tongue muscle structure. As such, the main goal of this research project was achieved. This conclusions chapter will summarize the steps leading up to achieving this goal and provide future directions.

Magnetic resonance imaging (MRI) was chosen as the primary paradigm for obtaining maps of 3D myoarchitecture because of its proven ability to image microstructure, and non-invasiveness. Imaging microstructure (10-20 μm) in MRI is possible through the use of diffusion weighted images, in which directions of less restricted diffusion correlate to statistically averaged fiber direction in an imaged voxel (1-5 mm). By understanding the equations of motion for spins, the diffusion weighted signal acquired in MRI is precisely quantifiable as a function of the probability distribution function (PDF) for diffusion. The most important feature of the PDF is that local maxima correlate with fiber directions, as was shown with simulated validation. DTI assumes that the PDF is an anisotropic Gaussian, which assumes that there is on a single fiber direction in a voxel. DSI and other high angular resolution diffusion techniques make no such assumption and allow for the possibility of multiple fiber directions in a voxel. Microfludic validation should have confirmed the ability of the DSI to resolve crossing fibers experimentally, but was unable to due to a

flawed pulse sequence. Finally the results using DTI and DSI in several cow tongues were presented confirming the crossing fiber structure of the core of the tongue, and the ability of DSI to resolve it. Tractography images are understood as intervoxel streamline connectivity of intravoxel fiber directions, and provide virtual anatomical displays of the complex myoarchitecture seen in the tongue.

For future directions of this research, there are several more key barriers to overcome. The foremost goal is to acquire images of myoarchitecture in-vivo. This is difficult due to the lengthy acquisition time for the typical 515 diffusion weighting directions used in DSI. Thus, in-vivo most likely requires a more limited q-space acquisition. DTI is slightly too limited because the tongue exhibits crossing fibers in the core. Other possibilities for the tongue in-vivo include q-ball imaging (which images only the surface of a sphere in q-space), higher order tensor imaging, and multitensor imaging. Consequently, since these techniques only sample a limited portion of q-space, it is important to know beforehand what the best portion of q-space to sample is. Microfluidic phantoms may help in this regard. Even with these techniques there is still core difficulty in dealing with the motion and susceptibility issues of the tongue. In-vivo imaging must be possible for mapping of 3D myoarchitecture to become clinically useful.

Another future direction is the correlation of myorachitecture data with strain data and finite element simulation of tongue mechanics. Strain data previously acquired for the tongue has been primarily 2D, with assumptions necessary to extrapolate to 3D. More recent strain imaging MRI sequences have made it possible to acquire full 3D strain and strain rate data in-vivo, but one main issue is that these techniques require repeatable motions with gated acquisitions. Finding what motions are repeatable and methods for gating still remain to be worked out. Finite element simulation should be able to infer material properties of the tissue from the 3D myoarchitecture as presented is this thesis. These simulations can be correlated with strain imaging data and used to infer the function in the tongue.

Thanks for reading.

<div style="text-align:center">The End</div>

Appendix A

Variables and Constants

Table A.1: The definitions of the math conventions used in this thesis.

Variable	Definition
$\vec{}$	vector
$\hat{}$	unit vector
bold face	second order tensor
$(\ )_i$ or $(\ )_{ij}$	components of vector or tensor
$\|\ \|$	magnitude of a vector
$\otimes$	tensor product (e.g. components of $\vec{a} \otimes \vec{b}$ are $a_i b_j$)
$\bar{(\ )}$	average
∇	gradient operator
∇^2	divergence of the gradient operator (i.e. diff grad *)
$'$	denotes a rotating coordinate system at the Larmor frequency
$\mathcal{F}$	Fourier transform

Table A.2: The definitions of variables and constants used in this thesis.

Variable	Definition
$\vec{}$	vector
$\hat{}$	unit vector
bold face	second order tensor
γ	proton gyromagnetic ratio $= 2.675 \times 10^8 \frac{\text{rad}}{\text{T}\cdot\text{s}}$
$\vec{B}$	magnetic field
$\vec{\mu}$	magnetic moment
$\vec{J}$	spin angular momentum, or spin
ν	Larmor frequency
V	unit volume
$\vec{M}$	averaged magnetization vector per unit volume
M_z	component of $\vec{M}$ in the z direction only
$\vec{M}_\perp$	components of $\vec{M}$ in the xy plane only
M_+	components of $\vec{M}_\perp$ written in terms of the complex plane
ω_0	precession frequency due to an applied $\vec{B}_0$ magnetic field
ω_1	precession frequency due to an applied $\vec{B}_1$ magnetic field
$\vec{g}$	magnetic field gradient of z direction magnetization
P	concentration, or equivalently probability distribution function
$\vec{r}$	position vector
$\vec{v}$	velocity vector $= \frac{d\vec{r}}{dt}$
t	time
D	diffusion tensor
δ	gradient pulse time
Δ	diffusion or mixing time
$\vec{q}$	q-value
$\vec{R}$	position vector from $\vec{r}$
λ_i	eigenvalues of **D**
PDF	same as P
ODF	orientational distribution function

Bibliography

[1] L. A. Aamport. The elephant's head. studies in the comparative anatomy of the head of the indian elephant and other mammals. *Part I. The facial muscles and the proboscis*, 41(7):1–79, July 1908. This is a full ARTICLE entry.

[2] S. Abd-El-Malkek. Observations on the morphology of the human tongue. *Journal of Anatomy*, 73:201–210, 1939.

[3] Y. M. Barnwell. Human lingual musculature: An historical review. *International Journal of Oral Myology*, 2:31–34, 1976.

[4] P. J. Basser. Fiber-tractography via diffusion tensor mri (dt-mri). In *Proceedings of 6th Annual Meeting ISMRM, Sydney*, page 1226, 1998.

[5] P. J. Basser. Relationships between diffusion tensor and q-space mri. *Magnetic Resonance in Medicine*, 47:392–397, 2002.

[6] P. J. Basser, J. Mattiello, and D. Lebihan. Mr diffusion tensor spectroscopy and imaging. *Biophysical Journal*, 66:259–267, 1994. eigensystem.

[7] R. A. Bergman, A. K. Afifi, and J. L. Bates. Atlas of human anatomy. Internet website, Accessed May 2005. http://www.vh.org/adult/provider/anatomy/atlasofanatomy/index.html.

[8] F. Bloch, W. W. Hansen, and M. Packard. The nuclear induction experiment. *Physical Review*, 70(7-8):474–485, 1946.

[9] R. Brown. A brief account of microscopical observations made in the months of june, july, and august 1827 on the particles contained in the pollen of plants;

and on th general existence of active molecules in organic and inorganic bodies. *Philosoph. Mag.*, 4:161, 1828.

[10] P. T. Callaghan. *Principles of nuclear magnetic resonance microscopy*. Oxford Press, Great Britain, 1993.

[11] D. G. Cory and A. N. Galloway. Measurement of translational displacement probabilities by NMR: An indicator of compartmentation. *Magn. Reson. Med.*, 14:435–444, 1990.

[12] R. Depaul and J. H. Abbs. Quantitative morphology and histochemistry of intrinsic lingual muscle fibers in macaca fascicularis. *Acta Anatomica*, 155:29–40, 1996.

[13] A. S. Gaunt and C. Gans. Serially arranged myofibers: An unappreciated variant in muscle architecture. *Experientia*, 48:864–868, 1989.

[14] A. S. Gaunt, G. E. Loeb, and F. de Vree. Architecture and consequent physiological properties of the semitendinosus muscle in domestic goats. *J. Morphol.*, 199:287–297, 1989.

[15] R. J. Gilbert, S. Daftary, T. G. Reese, R. M. Weisskoff, and V. J. Wedeen. Determination of lingual myoarchitecture in whole tissue by nmr imaging of anisotropic water diffusion. *Am. J. Physiol.*, 175:363–369, 1998.

[16] A. F. Gmitro and A. S. Alexander. Use of a projection reconstruction method to decrease motion sensitivity in diffusion weighted mri. *Magnetic Resonance in Medicine*, 29:835–838, 1993.

[17] E. L. Hahn. Spin echoes. *Phys. Rev.*, 80:580–602, 1950.

[18] J. V. Hajinal, A. S. Hall, A. G. Collins, A. Oatridge, J. M. Pennock, I. R. Young, and G. M. Bydder. Mr imaging of anisotropically restricted diffusion of water in the nervous system: technical, anatomic, and pathologic considerations. *Journal Computer Assisted Tomography*, 15:1–18, 1991.

[19] W. M. Kier and K. K. Smith. Tongues, tentacles and trunks: the biomechanics of movement in muscular-hydrostats. *Zoological Journal of the Linnean Society*, 83:307–324, 1985.

[20] P. C. Lauterbur. Image formation by induced local interactions: Examples employing nmr. *Nature*, 190:242, 1973.

[21] C. P. Lin, V. J. Wedeen, J. H. Chen, C. Yao, and W. Y. Tseng. Validation of diffusion spectrum magnetic resonance imaging with manganese-enhanced rat optic tracts and ex vivo phantoms. *Neuroimage*, 19(3):482–495, 2003.

[22] C. Liu, R. Bammer, B. Acar, and M. E. Moseley. Characterizing non-gaussian diffusion by using generalized diffusion tensors. *Magnetic Resonance in Medicine*, 51:924–937, 2004.

[23] P. Mansfield and P. K. Grannell. Nmr 'diffraction' in solids? *J. Phs. C: Solid State Phys.*, 6:L422, 1973.

[24] M. McLean and J. W. Prothero. Determination of relative fiber orientation in heart muscle: Methodologic problems. *Anatomical Record*, 232:459–465, 1991.

[25] P. P. Mitra and B. I. Halperin. Effects of finite gradient-pulse widths in pulsed-field-gradient diffusion measurements. *Journal of Magnetic Resonance, Series A*, 113:94–101, 1995.

[26] K. Miyawaki. A study of the musculature of the human tongue. *Annual Bulletin of the Research Institute of Logopedics and Phoniatrics - University of Tokyo*, 8:23–50, 1974.

[27] M. E. Moseley, Y. Cohen, J. Mintorovitch, L. Chileuittand, H. Shimizu, J. Kucharczyk, M. F. Wendland, and P. R. Weinstein. Early detection of regional cerebral ischemia in cats: comparison of diffusion- and t2-weigted mri and spectroscopy. *Magnetic Resonance in Medicine*, 14:330–346, 1990.

[28] M. E. J. Moseley, J. Kucharczyk, H. S. Asgari, and D. Norman. Anisotropy in diffusion-weighted mri. *Magnetic Resonance in Medicine*, 19:321–326, 1991.

[29] L. Mu and I. Sanders. Neuromuscular organization of the canine tongue. *Anat. Rec.*, 256:412–424, 1999.

[30] V. J. Napadow, Q. Chen, V. Mai, P. T. C. So, and R. J. Gilbert. Quantitative analysis of 3d resolved fiber architecture in heterogeneous skeletal muscle using nmr and optical imaging methods. *Biophys. J*, 80:2968–2975, 2001.

[31] V. J. Napadow, Q. Chen, V. J. Wedeen, and R. J. Gilbert. Intramural mechanics of the human tongue in association with physiological deformations. *J. Biomechanics*, 32:1–12, 1999.

[32] V. J. Napadow, R. D. Kamm, and R. J. Gilbert. A biomechanical model of sagittal tongue bending. *Journal of Biomechanical Engineering*, 124:547–556, 2002.

[33] K. C. Nishikawa, W. M. Kier, and K. K. Smith. Morphology and mechanics of tongue movement in the african pig-nosed hemisus marmoratum: A muscular hydrostatic model. *J. Exp. Biol.*, 202:771–780, 1999.

[34] E. M. Purcell, H. C. Torrey, and R. Pound. Resonance absorption by nuclear magnetic moments in a solid. *Physical Review*, 69(1):37–38, 1946.

[35] K. K. Smith and W. M. Kier. Trunks, tongues, and tentacles: moving with skeletons of muscle. *American Scientist*, 77:29–35, 1989.

[36] A. J. Sokoloff. Localization and contractile properties of intrinsic longitudinal motor units of the rat tongue. *J. Neurophysiology*, 84:827–835, 2000.

[37] C. F. Sonntag. The comparative anatomy of the tongues of mammalia. xii. summary, classification, and physiology. *Journal of Zoology: Proceedings of the Zoological Society of London*, 21:701–762, 1925.

[38] E. O. Stejskal. Use of spin echoes in a pulsed magnetic-field gradient to study anisotropic, restricted diffusion and flow. *The Journal of Chemical Physics*, 43(10):3597–3603, 1965.

[39] E. O. Stejskal and J. E. Tanner. Spin diffusion measurements: Spin echoes in the presence of a time-dependent field gradient. *The Journal of Chemical Physics*, 42(1):288–292, 1965.

[40] H. Takemoto. Morphological analyses of the human tongue musculature for three-dimensional modeling. *Journal of Speech, Language, and Hearing Research*, 44:95–107, 2001.

[41] D. G. Taylor and M. C. Bushell. The spatial mapping of translation diffusion coefficients by the nmr imaging technique. *Phys. Med. Biol.*, 30:345–349, 1985.

[42] H. C. Torrey. Bloch equations with diffusion terms. *Physical Review*, 104:563–565, 1956.

[43] D. S. Tuch. *Diffusion MRI of complex tissue structure*. PhD thesis, Massachusetts Institute of Technology, 2002.

[44] V. J. Wedeen, T. G. Reese, V. J. Napadow, and R. J. Gilbert. Demonstration of primary and secondary fiber architecture of the bovine tongue by diffusion tensor magnetic resonance imaging. *Biophys. J.*, 80:1024–1028, 2001.

[45] V. J. Wedeen, T. G. Reese, D. S. Tuch, M. R. Weigel, J. G. Dou, R. M. Weiskoff, and D. Chessler. Mapping fiber orientation spectra in cerebral white matter with fourier-transform diffusion MRI. In *Proceedings of 8th Annual Meeting ISMRM, Denver*, page 82, 2000.

[46] M. W. Westneat. Vertebrate functional morphology and phology. *Encyclopedia of Life Sciences*, 2001.

[47] J. C. Wu, E. C. Wong, E. L. Arrindell, K. B. Simons, A. Jesmanowicz, and J. S. Hyde. In vivo determination of the anisotropic diffusion of water and the t1

and t2 times in the rabbit lens by high-resolution magnetic resonance imaging. *Investigative Ophthalmology and Visual Science*, 34:2151–2158, 1993.